Earthquake ruptures with thermal weakening and the operation of major faults at low overall stress levels

Hiroyuki Noda,[1] Eric M. Dunham,[2] and James R. Rice[2]

[1]   We model ruptures on faults that weaken in response to flash heating of microscopic asperity contacts (within a rate-and-state framework) and thermal pressurization of pore fluid. These are arguably the primary weakening mechanisms on mature faults at coseismic slip rates, at least prior to large slip accumulation. Ruptures on strongly rate-weakening faults take the form of slip pulses or cracks, depending on the background stress. Self-sustaining slip pulses exist within a narrow range of stresses: below this range, artificially nucleated ruptures arrest; above this range, ruptures are crack-like. Natural earthquakes will occur as slip pulses if faults operate at the minimum stress required for propagation. Using laboratory-based flash heating parameters, propagation is permitted when the ratio of shear to effective normal stress on the fault is $0.2-0.3$; this is mildly influenced by reasonable choices of hydrothermal properties. The San Andreas and other major faults are thought to operate at such stress levels. While the overall stress level is quite small, the peak stress at the rupture front is consistent with static friction coefficients of $0.6-0.9$. Growing slip pulses have stress drops of ~ 3 MPa; slip and the length of the slip pulse increase linearly with propagation distance at ~ 0.14 and ~ 30 m/km, respectively. These values are consistent with seismic and geologic observations. In contrast, cracks on faults of the same rheology have stress drops exceeding 20 MPa, and slip at the hypocenter increases with distance at ~ 1 m/km.

1.   Introduction

1.1.   State of Stress on Faults

[2]   Understanding the stress levels at which faults operate remains an outstanding issue in earthquake mechanics. Laboratory friction experiments at slow slip rates, far less than coseismic rates of ~ 1 m/s, universally reveal friction coefficients, f, between 0.6 and 0.9 for almost all rock types (with the exception of clays and other weak layered minerals), a result known as Byerlee's law [*Byerlee*, 1978]. Assuming that pore pressure, p, is close to hydrostatic within the seismogenic upper crust, shear stress levels of ~ 100 MPa are required to bring faults into a critically stressed state. There are, however, a number of lines of evidence that indicate that major faults support and are capable of hosting self-sustaining ruptures when the overall (i.e., spatially averaged) ratio of shear stress, τ, to effective normal stress, $\overline{\sigma}$, is only a fraction of that predicted by Byerlee's law. This does not preclude the existence of small regions of locally high $\tau/\overline{\sigma}$, which are the likely sites of rupture nucleation.

[3]   It was recognized some time ago that frictional sliding of faults at such stresses should produce a heat signature that ought to be observable in the form of temperature anomalies across fault traces. The lack of observed temperature anomalies along the San Andreas Fault (SAF) places an upper bound on the average shear stress doing work during large seismic slips of ~ 10 MPa [*Brune et al.*, 1969; *Lachenbruch and Sass*, 1980; *Lachenbruch et al.*, 1995; *Williams et al.*, 2004]. While some have argued that groundwater flow might destroy the thermal signature of faulting at the stress levels predicted by Byerlee's law [*Scholz*, 2000], models of topologically driven flow along the SAF have shown that, at least along certain portions of the fault, this is unlikely to be the case [*Saffer et al.*, 2003].

[4]   Another set of constraints on the stress state on and around faults comes from in situ stress measurements (e.g., hydraulic fracturing and wellbore breakouts). Particular emphasis has been placed on determining the stresses acting on the SAF. Stresses adjacent to the SAF near Parkfield are consistent with a crust that is critically stressed at $f \sim 0.6-0.9$, but the stress field is oriented such that the ratio of shear stress to effective normal stress, $\tau/\overline{\sigma}$, resolved onto the SAF is quite low [*Zoback et al.*, 1987]. Measurements at 2 km depth in the San Andreas Fault Observatory at Depth (SAFOD) pilot hole, located 1.8 km from the trace of the SAF, indicate that the maximum horizontal compressive stress is inclined at $69 \pm 14°$ from the local strike of the SAF [*Hickman and Zoback*, 2004]. This is consistent with the

[1]Seismological Laboratory, California Institute of Technology, Pasadena, California, USA.
[2]Department of Earth and Planetary Sciences and School of Engineering and Applied Sciences, Harvard University, Cambridge, Massachusetts, USA.

orientation of the regional stress field in central and southern California, which is reported by *Townend and Zoback* [2004] to be $68 \pm 7°$. The high angle between maximum compression and the fault implies that $\tau/\overline{\sigma}$ resolved on the SAF is only 0.2–0.4 [*Hickman and Zoback*, 2004]. Similar results were found within the Cajon Pass borehole along the SAF [*Zoback and Healy*, 1992].

[5] The nearly fault-normal orientation of maximum horizontal compression explains the existence of folds and thrust faults that strike parallel to the SAF [*Mount and Suppe*, 1987]. Inversions for the orientation of the stress field from earthquake focal mechanisms are less conclusive, though the data appear to suggest angles of at least 40–60°, if not greater [*Hardebeck and Hauksson*, 2001; *Townend and Zoback*, 2001; *Provost and Houston*, 2001, 2003; *Hardebeck and Michael*, 2004]. *Scholz* [2006] and *Townend* [2006] provide recent reviews of the controversy surrounding the state of stress on the SAF that explore these issues in greater detail.

[6] A further difficulty with coseismic slip at $f \sim 0.6$–0.9 and hydrostatic p is that the predicted temperature rise on faults from shear heating will be sufficiently severe as to induce melting [*McKenzie and Brune*, 1972]. The temperature rises would be less extreme if slip were accommodated across a broad shear zone [*Cardwell et al.*, 1978], and this could possibly preclude melting. Yet recent fieldwork on exhumed faults like the Punchbowl fault [*Chester and Chester*, 1998; *Chester et al.*, 2004] and the Median Tectonic Line fault [*Wibberley and Shimamoto*, 2003] suggests a high degree of shear localization. Extreme localization within gouge layers during laboratory friction experiments has also been observed [*Beeler et al.*, 1996; *Mizoguchi and Shimamoto*, 2004]. Analysis of core retrieved from a drill hole across the Chelungpu fault, which hosted the 1999 M_w 7.6 Chi-Chi earthquake, suggests slip was accommodated within a clay zone only 50–300 μm thick [*Heermance et al.*, 2003]. *Sibson* [2003] and *Rockwell and Ben-Zion* [2007] discuss further field evidence for localization. *Rice* [2006] calculates that if sliding occurs at constant τ (with $f = 0.6$ and hydrostatic p that remains unchanged with slip), fault widths must exceed about 35 mm to prevent the onset of melting at 7 km depth [see also *Rempel and Rice*, 2006]. The observational signature of melting is the presence of pseudotachylytes in the fault zone. While pseudotachylytes have been observed along natural faults, they are generally associated with deeper faulting within the seismogenic zone and are far less common than expected [*Sibson*, 1975], so they either do not generally occur (at least near the surface) or are not preserved.

1.2. Weakening Mechanisms

[7] The scarcity of pseudotachylytes, despite the apparent thinness of the slip zone, suggests that coseismic slip occurs at much lower stress levels than those predicted by Byerlee's law. The explanation we consider in this study is that fault strength is dramatically reduced at coseismic slip rates (and that restrengthening occurs rapidly upon the cessation of slip). We do not discuss or intend to dismiss other possible resolutions of the stress level and heat flow issues, by assuming that fault materials have anomalously low f at all slip rates, or that f is not low but that p is near-lithostatic over much of the fault.

[8] Furthermore, our focus is on major faults. The stress measurements by *Townend and Zoback* [2000] make it clear that $\tau/\overline{\sigma}$ on optimally oriented planes within the crust frequently reaches typical static friction levels (0.6–0.9). It follows that overall stresses on many faults, especially those that are not major plate boundary faults, do operate at $\tau/\overline{\sigma} \sim 0.6$–$0.9$. Exactly why these faults do not rupture at lower stress levels like major faults remains unknown, but one might speculate that some of the assumptions we make in developing our model of major faults operating at low stress levels do not apply to less mature faults. For example, we appeal to a high degree of shear localization in developing our model of flash heating, which is the essential ingredient in permitting low stress ruptures. Immature faults consist of a large number of unconnected segments that ultimately link together as the fault develops [*Segall and Pollard*, 1983]. Likewise, measurements of fault surface topography by *Sagy et al.* [2007] suggest that faults become progressively smoother with increasing slip. The additional complexity of immature fault zones would likely increase the stress level necessary for ruptures to propagate and might help explain differences in stress levels at which immature and mature faults operate. However, a complete resolution of this issue is beyond the scope of this work.

[9] Recent high speed friction experiments show that f decreases roughly as the inverse of the sliding velocity, V, for V above $\sim$0.1 m/s [*Tsutsumi and Shimamoto*, 1997; *Tullis and Goldsby*, 2003a, 2003b; *Prakash and Yuan*, 2004; *Hirose and Shimamoto*, 2005; *Beeler et al.*, 2008]. This is presumably due to flash heating of microscopic asperity contacts, as first proposed in the field of dry metal friction [*Bowden and Thomas*, 1954; *Archard*, 1958/1959; *Ettles*, 1986; *Lim and Ashby*, 1987; *Lim et al.*, 1989; *Molinari et al.*, 1999] and recently applied to rock friction at elevated slip rates [*Rice*, 1999, 2006; *Beeler and Tullis*, 2003; *Beeler et al.*, 2008]. This model appeals to a microscopic view of friction, in which rough surfaces that are brought together make actual contact only at a set of microscopic asperities, the net area of which is a small fraction of the nominal contact area. These asperities come into existence and slide only a short distance before being replaced by a new set of contacts. The stresses supported by these asperities are far larger than the macroscopic applied stresses; hence, the local rate of heat production during sliding is quite large. If, during the lifetime of an asperity contact, the local temperature reaches the melting temperature (or some comparable temperature at which thermally activated defects become highly mobile), the contact will weaken. The macroscopic resistance to sliding is the sum over all currently existing contacts. The onset of strong weakening seen in experiments at $\sim$0.1 m/s is attributed to the slip rate reaching a critical value at which asperities just begin to weaken before sliding out of existence. At higher slip rates, the contacts spend a larger portion of their existence in the weakened state (such that at some instant, a larger fraction of currently existing contacts are in the weakened state).

[10] A second weakening mechanism involves fluids in fault zones. The majority of coseismic slip occurs below the water table, such that fault zones, to the extent that they are porous, should be fully saturated with pore fluid. As the fault slides, it heats both the rock matrix and pore fluid. Both materials expand, but the thermal expansion coeffi-

cient of water far exceeds that of rock. The stiffness of the rock matrix limits the expansion of the fluid, which consequently pressurizes. If the fault zone material is sufficiently impermeable, then this pressurized fluid is effectively trapped over the duration of coseismic slip. The increase in fluid pressure decreases effective stress and hence fault strength. This process, known as thermal pressurization, has received considerable theoretical attention [*Sibson*, 1973; *Lachenbruch*, 1980; *Mase and Smith*, 1985, 1987; *Lee and Delaney*, 1987; *Andrews*, 2002, 2005; *Wibberley*, 2002; *Noda*, 2004; *Cocco and Bizzarri*, 2004; *Noda and Shimamoto*, 2005; *Sulem et al.*, 2005; *Bizzarri and Cocco*, 2006a, 2006b; *Suzuki and Yamashita*, 2006; *Rice*, 2006; *Rempel and Rice*, 2006].

[11] Even if flash heating and/or thermal pressurization weaken faults and reduce heat production, a sufficiently long duration of sliding may result in macroscopic melting of rock and formation of a molten layer along the sliding interface; the ultimate fate of a fault zone for large amounts of slip depends on thermal and hydraulic parameters (e.g., permeability of fault gouge), as well as the initial effective normal stress and sliding rate [*Rempel and Rice*, 2006]. The onset of melting and its effect on fault strength, as well as the characterization of naturally occurring pseudotachylytes, has been the subject of much work [*Sibson*, 1975; *Spray*, 1987, 1992, 1993, 1995; *Tsutsumi and Shimamoto*, 1997; *Matsuzawa*, 2004; *Fialko and Khazan*, 2004; *Hirose and Shimamoto*, 2005; *Di Toro et al.*, 2006; *Sirono et al.*, 2006; *Nielsen et al.*, 2008].

[12] Several other processes have been suggested to influence fault strength during earthquakes. These include elastohydrodynamic lubrication (due to pressure gradients established by viscous shear of fault zone fluids or a melt layer trapped between the walls of the fault) [*Brodsky and Kanamori*, 2001] and silica gel formation [*Goldsby and Tullis*, 2002; *Di Toro et al.*, 2004]. Silica gel formation is likely restricted to faults in silica-rich host rock (e.g., granite), and gel lubrication, like thermal decomposition weakening [*Han et al.*, 2007] and formation of a macroscopic melt layer, would only take place after sufficiently large slip, if at all. Thus we assume that the most universal mechanisms, especially during the early stages of rupture growth, are likely to be thermal pressurization and flash heating, which are the two processes that we study on in this work.

1.3. Rupture Modes on Statically Strong, Dynamically Weak Faults

[13] In light of the above discussion, the task before us is to reconcile laboratory observations that indicate rock friction coefficients between 0.6 and 0.9, at slow slip speeds, with the multiple lines of evidence suggesting that average stress levels on major faults are much smaller than those predicted by Byerlee's law. The hypothesis that we explore in this work is that faults are strong throughout the interseismic period, but weaken dramatically (by the mechanisms discussed previously) when sliding coseismically, a process referred to as dynamic weakening. *Lapusta and Rice* [2003] have shown, in earthquake cycle simulations that simultaneously incorporate slow loading in the interseismic period and fully elastodynamic coseismic ruptures, how faults having a shear strength that weakens dramatically

with slip rate can host ruptures when the average shear stress on the fault is quite low. The low shear strength during coseismic slip results in minimal heat production.

[14] Intimately related to the concept of strongly rate-weakening faults, operating at low overall stress levels, is that ruptures take the form of self-healing slip pulses. There is strong observational support that ruptures propagate as slip pulses; slip inversions of high frequency seismic signals indicate that risetimes are much shorter than event durations [*Heaton*, 1990]. Three mechanisms have been shown to produce slip pulses: a contrast in material properties across the fault [*Andrews and Ben-Zion*, 1997], arrest waves from fault edges or from heterogeneity along the fault [*Day*, 1982; *Johnson*, 1990; *Beroza and Mikumo*, 1996; *Bizzarri et al.*, 2001], and velocity weakening constitutive laws on understressed faults [*Cochard and Madariaga*, 1994, 1996; *Perrin et al.*, 1995; *Beeler and Tullis*, 1996; *Zheng and Rice*, 1998].

[15] *Zheng and Rice* [1998] studied rupture propagation using rate- and state-dependent friction laws featuring velocity-weakening steady state fault strengths. They showed that when fault strength weakens sufficiently rapidly with slip velocity, there exists a critical background shear stress level, τ^{pulse}, below which ruptures must take the form of slip pulses. For background stresses above τ^{pulse}, ruptures can also take the form of expanding cracks (in the sense that slip near the hypocenter does not cease until the arrival of arrest waves emitted when the rupture reaches the fault edges). Self-sustaining slip pulses were found to exist only when stresses are right around τ^{pulse}; at much lower stress levels, artificially nucleated ruptures quickly arrest. It follows that quasi-statically loaded faults are capable of hosting ruptures (in the sense that an initially small event, nucleated in a region of locally high $\tau/\overline{\sigma}$, can propagate indefinitely) just as stresses reach the minimum level necessary for self-sustaining rupture propagation. At this level, ruptures will take the form of slip pulses. Earthquake cycle simulations by *Lapusta and Rice* [2003] which incorporate a steady state friction coefficient that weakens dramatically at coseismic slip rates, support this claim. Lapusta and Rice further demonstrate that nucleation occurs in small regions where $\tau/\overline{\sigma}$ locally exceeds $\tau^{\text{pulse}}/\overline{\sigma}$ based on the average $\overline{\sigma}$ on the fault, and reaches levels comparable to those predicted using laboratory values of static friction. In our work, we also focus on faults that dramatically weaken at coseismic slip rates, but we incorporate a far more sophisticated, physics-, field-, and laboratory-based description of the dynamic weakening processes (in particular, flash heating and thermal pressurization). The combined effect of these weakening mechanisms cannot be written in a form that permits direct application of the theory by *Zheng and Rice* [1998] and extending their theory to encompass a broader set of constitutive laws is an additional focus of our work.

1.4. Overview

[16] In this study, we present a theoretical model that addresses the issues discussed, and we numerically simulate spontaneous ruptures on faults that weaken by flash heating and thermal pressurization. We use a combination of laboratory and field data to constrain the relevant thermal and hydraulic properties that enter the model, and explore the

Table 1. Physical Properties and Model Parameters

Elastic Properties		
Shear modulus	μ	30 GPa
Shear wave speed	c_s	3 km/s
Hydrothermal Properties		
Specific heat[a]	ρc	2.7 MJ/m^{3}K
Thermal diffusivity[a]	α_{th}	0.7 mm^2/s
Hydraulic diffusivity[a]	α_{hy}	0.86–3.52 mm^2/s
Undrained $\Delta p/\Delta T$[a]	Λ	0.34–0.98 MPa/K
Damage index[a]	r	0–1
Width of shear zone	$2w$	25–200 μm
Friction (Flash Heating)		
Unweakened contact strength	τ_c	3 GPa
Weakening temperature	T_w	900°C
Asperity diameter	D	5 μm
Fully weakened friction coefficient[b]	f_w	0.13
Friction (Rate and State)		
Reference slip velocity	V_0	1 μm/s
Steady state friction coefficient at V_0	f_0	0.7
State evolution distance	L	20 μm
Direct effect parameter	a	0.016
Evolution effect parameter	b	0.02
Initial Conditions		
Normal stress	σ	196 MPa
Initial pore pressure	p_0	70 MPa
Initial temperature	T_0	210°C
Resulting initial V_w	V_{w0}	0.170 m/s
Initial state variable	Θ_0	0.59211
Background shear stress	τ^b	24–35 MPa
Initial τ at hypocenter	$\tau^b + \tau^{per}$	100–150 MPa
Width of perturbation	D^{per}	1–3 cm

[a]Data compiled by *Rice* [2006, Table 2] for ambient T and p at 7-km depth.

[b]From curve fit to data up to $V = 0.4$ m/s from experiments on granite by *Tullis and Goldsby* [2003b].

phenomenology of ruptures initiated by an artificial nucleation mechanism (classifying them as arresting slip pulses, growing slip pulses, and growing cracks). Because we make no compromises in physical parameters, our numerical simulations require incredibly small grid spacings for accurate solutions. We consequently limit our simulations to two-dimensional (mode III) ruptures and focus on the early stages of rupture growth. The strong velocity-weakening behavior of flash heating promotes self-healing slip pulses on faults with sufficiently low values of initial $\tau/\overline{\sigma}$; growing pulses occur when $\tau/\overline{\sigma} \sim 0.2$–0.3. These values are consistent with those inferred to act on the SAF [*Hickman and Zoback*, 2004] (and presumably other major faults). Thermal pressurization can alter the rupture mode; efficient pressurization (occurring on more impermeable faults) extends the crack-like rupture regime to lower values of $\tau/\overline{\sigma}$ than those predicted by flash heating alone, though the background stress level remains the dominant predictor of rupture mode. We also find that the width of the shear zone influences the rupture mode, and that there are major differences (primarily with regard to maximum temperatures and pressures achieved at the rupture front) between models in which shear is distributed over 50–200 μm and the idealized model of slip on a mathematical plane discussed by *Rice* [2006]; that such small but nonzero thicknesses might be important in limiting maximum

temperatures was also suggested by *Rice* [2006] and *Rempel and Rice* [2006].

2. Model

[17] Since our focus is on rupture propagation with dynamic weakening mechanisms, we choose to study ruptures in a setting for which the elastic response is easily understood. Furthermore, our direct use of laboratory and field estimates of relevant parameters requires us to use very small grid spacings compared to the propagation distances of interest. Consequently, we study two-dimensional, mode III ruptures in a uniform linear elastic whole space. The medium has shear modulus μ and shear wave speed c_s. The fault lies along the plane $z = 0$. Slip is in the y direction, the rupture expands outward along the x axis, and all fields are functions only of x and z (and time, t). Initial stress, pore pressure, and material properties (to be discussed in the subsequent sections) are chosen to be representative of conditions at midseismogenic depth (7 km) and, in all cases, properties are chosen for consistency with laboratory constraints. These are given in Table 1 and are defined precisely in the following sections.

[18] Ruptures propagate in response to changes in shear strength, τ, which is given by

$$\tau = f(\sigma - p) = f\overline{\sigma} \tag{1}$$

where f is the friction coefficient, σ is total normal stress, p is pore pressure, and $\overline{\sigma}$ is effective normal stress. Both σ and $\overline{\sigma}$ are positive in compression, and all fields in (1) are evaluated on $z = 0$, even when shear is distributed over a finite region. The friction coefficient depends on slip velocity, V, as well as on internal state variables, as described later.

2.1. Flash Heating of Microscopic Asperity Contacts

[19] In this work we use the flash heating model by *Rice* [1999, 2006], *Beeler and Tullis* [2003], *Tullis and Goldsby* [2003a, 2003b], and *Beeler et al.* [2008], which provides a model for $f_{ss}(V, T)$. Suppose all asperities have length D, so that when sliding at constant V, they disappear at time $\theta_{max} = D/V$ after their birth. With a constant contact shear strength, τ_c, which *Rice* [2006] argues to be about the theoretical strength of the material, $\sim 0.1\mu = 3$ GPa, solving a one-dimensional heat conduction problem yields the temperature history of the contact:

$$T_c = T + \frac{\tau_c V \sqrt{\theta}}{\rho c \sqrt{\pi \alpha_{th}}}, \tag{2}$$

where θ is the contact time, T_c is the contact temperature, and T is the initial temperature, which is assumed to be equal to the macroscopic, or spatially averaged background, temperature on the fault. The macroscopic temperature changes much more slowly than T_c does since the actual contact area at asperities, A_c, is much smaller than the macroscopic, or nominal, surface area, A. This makes the rate of heat production per unit surface area at the contacts, $\tau_c V$, locally much higher than the average heating rate per unit surface area at the macroscopic scale, τV. However, there is consistency between the microscopic and macro-

scopic scales: the rate of thermal energy production at the scale of the asperities, $\tau_c A_c V$, is identical to that at the macroscopic scale, $\tau A V$.

[20] Assuming that weakening occurs when T_c reaches the weakening temperature, T_w, asperities are weakened at the age of

$$\theta_w = \frac{\pi \alpha_{th}}{V^2} \left(\frac{T_w - T}{\tau_c / \rho c} \right)^2. \tag{3}$$

In order for asperities to be weakened during their lifetime, $\theta_w \le \theta_{\max}$; it follows that the strict equality, $\theta_w = \theta_{\max}$, can be solved for the weakening velocity, V_w, above which flash heating is activated [Rice, 1999, 2006]:

$$V_w(T) = \frac{\pi \alpha_{th}}{D} \left(\frac{T_w - T}{\tau_c / \rho c} \right)^2. \tag{4}$$

As we have made explicit in the above expression, V_w is not constant because the background temperature T evolves during our dynamic calculations. We use the following parameter values: $D = 5$ μm, $T_w = 900°$C, $\tau_c = 3$ GPa, $\alpha_{th} = 0.70$ mm²/s, and $\rho c = 2.7$ MPa/K (the choice of α_{th} and ρc is discussed in the following section on thermal pressurization). For an initial background temperature of $T_0 = 210°$C, the initial weakening slip rate, V_{w0}, is 0.170 m/s (the subscript 0 denotes an initial value).

[21] Once the contact temperature of an asperity reaches T_w, we use the simple approximation in which contact shear strength drops abruptly at the onset of flash heating from τ_c to a constant weakened value, τ_{cw}. Dividing τ_c and τ_{cw} by the effective normal stress at the contacts gives the friction coefficients f_{LV} and f_w, respectively (where the subscript LV denotes low velocity, referring to $V < V_w$). In the previous derivation of $V_w(T)$, we assumed for simplicity that τ_c was constant. Treating τ_c as constant implies that f_{LV} is also constant if there is no change in the real contact area. It is well known experimentally that f_{LV} is mildly sensitive to V. Additionally, there are theoretical reasons, related to consideration of sliding as a process involving thermally activated defect motion at asperity contacts, that suggest a weak relationship between τ_c and V [Rice et al., 2001]. We employ a conventional logarithmic velocity-weakening model at steady state for f_{LV}:

$$f_{LV}(V) = f_0 + (a - b)\ln(V/V_0) \tag{5}$$

with $f_0 = 0.7$, $V_0 = 1$ μm/s, and $b - a = 0.004$.

[22] The use of a nonzero friction coefficient, f_w, at elevated slip rates in the model of Rice [1999] was introduced by Beeler and Tullis [2003], Tullis and Goldsby [2003a, 2003b], and Beeler et al. [2008], who found its inclusion necessary to better match their experimental data. We use $f_w = 0.13$, which is obtained by fitting to their granite data.

[23] The friction coefficient in our flash heating model is then obtained by averaging strength over the existing set of asperities. This means that when a single contact experiences an instantaneous reduction in strength upon reaching the weakening temperature, the macroscopic strength is only infinitesimally altered. In the steady state limit, the average over the current contact population is equivalent to averaging over contact lifetime. This procedure yields [Rice, 1999, 2006]:

$$f_{ss}(V, T) = \begin{cases} f_{LV}(V), & \text{if } V \le V_w \\ f_w + [f_{LV}(V) - f_w][V_w(T)/V], & \text{if } V \ge V_w. \end{cases}$$

Using purely velocity-weakening constitutive models leads to ill-posedness in problems of frictional sliding between elastic materials [Rice et al., 2001], so we are compelled not to ignore known experimental friction behavior, with regularizing properties, of the direct effect and state evolution. We add these features to this model before using it in our simulations. In particular, we use the slip-law formulation of rate-and-state friction [Dieterich, 1979; Ruina, 1983] in the form [Rice, 1983]:

$$\frac{df}{dt} = \frac{a}{V}\frac{dV}{dt} - \frac{V}{L}[f - f_{ss}(V, T)], \tag{7}$$

or in an integrated form:

$$f(V, \Theta) = a\ln(V/V_0) + \Theta$$
$$\frac{d\Theta}{dt} = -\frac{V}{L}[f(V, \Theta) - f_{ss}(V, T)], \tag{8}$$

where a is the nondimensional direct effect parameter (the same a as in the low velocity friction model), L is the state evolution distance, V_0 is an arbitrary reference slip velocity (we use the same value as appears in the expression for $f_{LV}(V)$), and Θ is the state variable as defined by Nakatani [2001]. The advantage of equation (8) over equation (7) is that equation (8) is slightly easier to deal with numerically (see appendices for details of the numerical procedure). As formulated above, these laws diverge at $V = 0$. If we understand frictional sliding as arising from a set of thermally activated processes, with stress-biased activation energies, at microscopic asperity contacts, then the logarithmic form of the law that we use here only accounts for the statistically more likely jumps in the direction of the applied stress. It is possible to regularize the response at $V = 0$ by including jumps in the opposite direction, as discussed by Lapusta et al. [2000]. We ran a few simulations using the regularized law, but the results were identical (to machine precision) to results using the unregularized law, as expected due to the infinitesimally small probabilities associated with backward jumps at the stress levels occurring in the simulations.

[24] The fraction of unweakened asperity area decreases with increasing slip velocity, implying that the contribution to the direct effect from those unweakened asperities also decreases. There are currently no experiments to constrain the transient evolution of the friction coefficient at coseismic slip rates, but Rice et al. [2001] point out that under the assumption that the direct effect arises from thermally activated shearing processes at asperity contacts, a should be linearly proportional to the absolute temperature at the contacts. In this work we use $a = 0.016$, which is obtained by linear extrapolation with absolute temperature from a typical value of 0.01 at room temperature [Ruina, 1983]. We also tried simulations in which we permitted a to vary as a

function of T, but found little difference with simulations employing a constant a.

[25] We use a state evolution distance, L, comparable to the asperity diameter, D, under the assumption that sliding a distance D refreshes all contacts. Specifically, we use $L = 20\ \mu$m for most of our simulations, although this requires an extremely small grid size to achieve an appropriate level of numerical accuracy. The high velocity friction experiments of *Prakash and Clifton* [1992] and *Prakash* [1998] show that, following extremely abrupt normal stress steps, f evolves toward its steady state value over slip distances around ∼3 μm; however, to date, no experiments have investigated the transient evolution of f following velocity steps at coseismic speeds. Furthermore, theoretical work by *Noda* [2008] implies that the evolution distance for flash heating may be much smaller than D. Suppose we keep the background temperature, T, constant by cooling, and impose steps in V for a fault comprised of single-sized asperities. Since all the asperities are renewed after slipping by D, evolution to the new steady state is perfectly achieved at a slip of D; it follows that L must be a fraction of D. Such small values of L are very difficult to use in simulations of rupture propagation. In addition, the flash heating constitutive law has a very high maximum weakening rate, $-\partial f_{\mathrm{ss}}(V, T)/\partial(\ln V)$, at V just above V_{w}.

[26] In the above discussion, we have implicitly assumed that flash heating occurs on a mathematically planar fault, while many lines of evidence suggest that seismic shear is distributed over a zone of remarkably small but nevertheless finite width. There have been several attempts to understand the microscopic picture of a rapidly sheared gouge layer by means of the distinct element method. *Morgan and Boettcher* [1999] observed development of shear planes where deformation is localized, and *da Cruz et al.* [2005] reported that only about 15% of all contacts are slipping at a given time. These works suggest that intergranular slip occurs at a small number of the contacts, and the local slip rate is about the same as the macroscopic slip rate of the fault. On the other hand, there are observations of thin but finitely thick shear zones in both exhumed faults [*Chester and Chester*, 1998; *Chester and Goldsby*, 2003; *Chester et al.*, 2004; *Heermance et al.*, 2003; *Mizoguchi and Shimamoto*, 2004] and specimens after frictional experiments at high slip rates [*Beeler et al.*, 1996; *Mizoguchi and Shimamoto*, 2004]. These shear zones are recognized by shape-preferred orientations of platy minerals, which clearly indicate that the total shear strain is distributed within it. Many of these studies suggest that shear localizes to zones of width ∼100 μm; see *Rice* [2006] for further discussion. In this work, our flash heating model is based on slip on a mathematical plane and we use the value of T at $z = 0$ when evaluating $f_{\mathrm{ss}}(V, T)$; however, we distribute the heat source over a finite width shear zone when calculating T and p changes in our thermal pressurization calculation. This approach is appropriate if, at any instant in time, only a small fraction of the contacts are slipping, and if the location of such slipping contacts moves around within the shear zone. In this case, the texture of severe shear deformation is developed over the distributed shear zone. It is also required that the timescale over which the localized slip surface migrates through the shear zone is much smaller than relevant thermal and hydraulic diffusion times.

2.2. Thermal Pressurization of Pore Fluid

[27] Thermal pressurization of pore fluid suppresses the temperature rise within and near the shear zone by reducing the effective normal stress and thus shear strength. This mechanism has been implemented in rupture propagation calculations by several authors [*Andrews*, 2002; *Noda*, 2004; *Cocco and Bizzarri*, 2004; *Andrews*, 2005; *Bizzarri and Cocco*, 2006a, 2006b; *Suzuki and Yamashita*, 2006] but never in combination with flash heating or other strongly velocity-weakening friction laws.

[28] The governing equations are those of energy and fluid mass conservation, along with Fourier's law and Darcy's law [e.g., *Rice*, 2006; *Rempel and Rice*, 2006]:

$$\rho c \frac{\partial T}{\partial t} = \frac{\partial}{\partial z}\left(K \frac{\partial T}{\partial z}\right) + \omega(z, t) \qquad (9)$$

$$\rho_f \beta \left(\frac{\partial p}{\partial t} - \Lambda \frac{\partial T}{\partial t}\right) = \frac{\partial}{\partial z}\left(\frac{\rho_f k}{\eta_f}\frac{\partial p}{\partial z}\right), \qquad (10)$$

in which ρc is the volumetric heat capacity of the gouge, K is thermal conductivity, ρ_f is fluid mass density, β is a storage coefficient, Λ is the pore pressure change per unit temperature change under undrained conditions, k is permeability, and η_f is fluid viscosity. β and Λ are more precisely defined in terms of the compressibilities and thermal expansivities of the pores and pore fluid, as discussed in greater detail by *Rice* [2006]. Shear heating enters as $\omega(z, t)$, the volumetric heat generation rate (taken as $\omega(z, t) = \tau(t)\ \dot{\gamma}(z, t)$, where $\dot{\gamma}(z, t)$ is the shear strain rate within the fault). Advective transport is neglected, which has been shown to be an accurate approximation if permeability is less than 10^{-16} m^2 [*Lachenbruch*, 1980; *Mase and Smith*, 1987; *Lee and Delaney*, 1987].

[29] The temperature and pressure dependence of several properties (e.g., k and ρ_f) makes these equations nonlinear, but simple estimates suggest that if the properties are expanded about representative values of T and p, the resulting nonlinear terms in the governing equations are almost always small compared to terms that are linear in T and p. Using numerical simulations that included all terms in the conservation equations, *Vredevoogd et al.* [2007] has demonstrated that nonlinear terms may be safely neglected for a physically reasonable range of parameters. In this study, we use the linearized form of the equations:

$$\frac{\partial T}{\partial t} = \alpha_{th}\frac{\partial^2 T}{\partial z^2} + \frac{\omega(z, t)}{\rho c} \qquad (11)$$

$$\frac{\partial p}{\partial t} = \alpha_{hy}\frac{\partial^2 p}{\partial z^2} + \Lambda \frac{\partial T}{\partial t}, \qquad (12)$$

in which $\alpha_{th} = K/(\rho c)$ is the thermal diffusivity and $\alpha_{hy} = k/(\beta \eta_f)$ is the hydraulic diffusivity. *Rice* [2006] and *Rempel and Rice* [2006] provide estimates of the average values of α_{hy} and Λ over the substantial temperature and pressure ranges that are likely to be experienced by fault gouge during seismic shear, and we use these path-averaged values

in our simulations. *Rempel and Rice* [2006] have shown that the linear formulation using these values gives a reasonable match to fully nonlinear calculations.

[30] We primarily consider a shear zone of small but finite thickness, but also investigate the limit of slip on a plane. For the case of distributed shear, we assume that the shear strain rate has a Gaussian profile, such that shear heating is given by

$$\omega(z,t) = \frac{\tau(t)V(t)}{w\sqrt{2\pi}} \exp\left(-\frac{z^2}{2w^2}\right), \tag{13}$$

where w is the half-width of the shear zone.

[31] *Rice* [2006] provides an analytical solution to equations (11) and (12) assuming that sliding commences at $t = 0$ and the fault slides forever after at constant V and f, in the limit that shear is localized on a mathematical plane ($w \rightarrow 0$):

$$T(0,t) = T_0 + \left(1 + \sqrt{\frac{\alpha_{hy}}{\alpha_{th}}}\right) \\ \cdot \frac{\overline{\sigma}_0}{\Lambda}\left[1 - \exp\left(\frac{Vt}{L_*}\right)\mathrm{erfc}\left(\sqrt{\frac{Vt}{L_*}}\right)\right], \tag{14}$$

$$p(0,t) = p_0 + \overline{\sigma}_0\left[1 - \exp\left(\frac{Vt}{L_*}\right)\mathrm{erfc}\left(\sqrt{\frac{Vt}{L_*}}\right)\right], \tag{15}$$

$$\tau(t) = f\overline{\sigma}_0 \exp\left(\frac{Vt}{L_*}\right)\mathrm{erfc}\left(\sqrt{\frac{Vt}{L_*}}\right), \tag{16}$$

where the subscript 0 denotes an initial value at $t = 0$. L_* is identified as the characteristic slip distance for temperature and pore pressure evolution due to thermal pressurization, defined by

$$L_* = \frac{4}{f^2 V}\left[\left(\frac{\rho c}{\Lambda}\right)^2 \left(\sqrt{\alpha_{th}} + \sqrt{\alpha_{hy}}\right)^2\right] = \frac{4}{f^2 V}\alpha_{HT}, \tag{17}$$

in which we define the term in brackets as α_{HT}, which we term the hydrothermal diffusivity factor; it has the virtue of being solely a function of the material properties of the surrounding rock (unlike L_*, which depends also on the assumed values of f and V). This solution also approximates the fields away from the fault for the case of a finite shear zone after the diffusion lengths become much larger than the width of the shear zone, as discussed by *Rempel and Rice* [2006]. The significance of (16) is that, strictly speaking, the steady state frictional shear stress is zero regardless of the fixed V, and that the apparent characteristic weakening displacement is a good fraction of total slip [*Rice*, 2006, Figure 3].

[32] *Rempel and Rice* [2006] and *Rice* [2006] estimated hydrothermal properties based on a collection of experimental and theoretical works [*Burnham et al.*, 1969; *Keenan et al.*, 1978; *Lachenbruch*, 1980; *Tödheide*, 1972; *Vosteen and Schellschmidt*, 2003; *Wibberley*, 2002; *Wibberley and Shimamoto*, 2003] for intact and damaged elastic fault walls composed of ultracataclasite at 7 km depth, 196 MPa normal stress, an ambient pore pressure of 70 MPa, and an ambient temperature of 210°C [see Table 2 in *Rice*, 2006]. These values are ρc = 2.7 MPa/K, Λ = 0.98 (intact) and 0.32 (damaged) MPa/K, α_{th} = 0.70 mm^2/s, α_{hy} = 0.86 (intact) and 3.52 (damaged) mm^2/s, which yield α_{HT} = 23.6 (intact) and 464.1 (damaged) mm^2/s. The hydraulic properties of rock are from the Median Tectonic Line fault in southwest Japan [*Wibberley*, 2002; *Wibberley and Shimamoto*, 2003]. The properties are summarized in Table 1.

[33] There is considerable uncertainty in choosing the appropriate value of permeability. *Wibberley and Shimamoto* [2003] measured permeability using nitrogen gas as the pore fluid, and *Faulkner and Rutter* [2000, 2003] showed for that for nonswelling clays the water permeability can be an order of magnitude smaller than the gas permeability. Permeability in and around fault zones can also be quite anisotropic with respect to the direction of flow relative to foliation of the gouge. *Faulkner and Rutter* [1998] found variations over three orders of magnitude with direction relative to the fault; the lowest permeability is typically that perpendicular to the fault, which is the relevant direction for our models. Additionally, studies of clayey gouge from the Neodani [*Tsutsumi et al.*, 2004] and Hanaore [*Noda and Shimamoto*, 2005] faults in southwest Japan, and the Chelungpu fault in Taiwan [*Tanikawa and Shimamoto*, 2009] yielded much higher permeabilities (10^{-19} to 10^{-16} m^2 at around 100 MPa effective pressure) than those measured by *Wibberley and Shimamoto* [2003] with the same methodology. The clayey gouge in these works typically contains a swelling clay for which the difference in gas and water permeability can be much greater than that estimated by *Faulkner and Rutter* [2000, 2003].

[34] As a consequence of the uncertainty in permeability measurements and in knowledge of how permeability and storage coefficients are affected by dynamic fracturing of the fault walls during rupture, two of the least constrained model parameters are the hydraulic parameters, α_{hy} and Λ. We study a range of these parameters by varying the two parameters together using a linear interpolation between intact and damaged values:

$$\alpha_{hy} = (0.86 + 2.66r)\mathrm{mm}^2/\mathrm{s} \tag{18}$$

$$\Lambda = (0.98 - 0.64r)\mathrm{MPa/K}, \tag{19}$$

where r is the nondimensional damage index, $0 \le r \le 1$.

[35] Previous studies [*Noda*, 2004; *Cocco and Bizzarri*, 2004; *Andrews*, 2005; *Bizzarri and Cocco*, 2006a, 2006b; *Suzuki and Yamashita*, 2006] typically used shear zones that are a few centimeters thick. However, observational studies of exhumed faults [*Chester and Chester*, 1998; *Chester et al.*, 2004; *Heermance et al.*, 2003; *Mizoguchi and Shimamoto*, 2004] and specimens after rotary shear experiments [*Beeler et al.*, 1996; *Mizoguchi and Shimamoto*, 2004] suggest that shear deformation is extremely concentrated in zones that are at most ~200 μm in width (and there is no evidence that rules out the possibility that at any instant, shear is localized in an even narrower zone). In this study we use at most $2w = 200$ μm. In our numerical simulations,

we integrated equations (11) and (12) using a conventional second-order finite difference method (in space) on a one-dimensional grid perpendicular to the fault plane at every node on the fault. Time stepping was performed using an adaptive Runge-Kutta method [*Dormand*, 1996]. Details of the numerical method are given in the appendices.

[36] There are experimental studies [*Linker and Dieterich*, 1992; *Prakash and Clifton*, 1992; *Prakash*, 1998; *Richardson and Marone*, 1999; *Bureau et al.*, 2000; *Boettcher and Marone*, 2004; *Hong and Marone*, 2005] on the memory effect in the response of shear strength to variations in normal stress that might cause one to question the validity of equation (1). *Linker and Dieterich* [1992] suggest that on a sudden jump in normal stress by $\Delta\overline{\sigma}$ during sliding, only a fraction of the expected shear stress change, $f\Delta\overline{\sigma}$, occurs immediately; this instantaneous response is followed by a gradual evolution toward the new steady state shear stress. However, while well supported experimentally at speeds less than ~1 mm/s, no instantaneous change in strength was noted following extremely abrupt steps in normal stress at the high speeds (~1–10 m/s) that occur coseismically [*Prakash and Clifton*, 1992; *Prakash*, 1998]. We also tested laws consistent with the Prakash–Clifton experiments by replacing equations (1) and (7) with

$$\frac{d\tau}{dt} = \frac{a\overline{\sigma}}{V}\frac{dV}{dt} - \frac{V}{L}[\tau - f_{ss}(V, T)\overline{\sigma}]. \qquad (20)$$

There was little difference from the cases in which τ was instantaneously coupled to $\overline{\sigma}$, presumably because the state evolution time, L/V, was small compared to the timescale, set by thermal and hydraulic diffusion, over which $\overline{\sigma}$ varied.

2.3. Predicted Background Stress Levels Separating Pulses and Cracks (Constant *T* and *p*)

[37] As discussed before, friction laws having strong velocity-weakening behavior (like flash heating) can cause ruptures to take the form of self-healing slip pulses, provided that the background shear stress level is below a critical level termed τ^{pulse} by *Zheng and Rice* [1998]. To begin, we consider faults with a steady state strength that depends only on *V*. In the context of our model, we do this by holding the background temperature, *T*, and pore pressure, *p*, fixed at their initial values, such that the steady state strength is $\tau_{ss}(V) = \overline{\sigma}_0 f_{ss}(V, T_0)$. In the following, we recall the results of *Zheng and Rice* [1998].

[38] A crack-like rupture is defined as one in which points on the fault that have started sliding (e.g., the hypocenter) continue to slide until arrest waves from the edges of the fault (or strong heterogeneities on the fault) arrive and cause the fault to lock. This prompts us to ask, under what conditions does there exist a nonzero slip velocity, *V*, that simultaneously satisfies the friction law and the elastodynamic equation? If no such solution exists, then the fault must lock and ruptures, if they exist, must take the form of self-healing slip pulses. For this analysis, it is most convenient to express the elastodynamic equation in the form of a boundary integral equation. For a planar fault in a homogeneous two-dimensional medium, this is

$$\tau(x, t) = \tau_0(x, t) - \frac{\mu}{2c_s}V(x, t) + \phi(x, t), \qquad (21)$$

in which $\tau_0(x, t)$ is the shear stress in the absence of slip and $\phi(x, t)$ is the stress transfer functional (i.e., the stress carried by elastic waves [*Perrin et al.*, 1995; *Geubelle and Rice*, 1995]). Physically, equation (21) states that the stress at some point on the fault is equal to the load, $\tau_0(x, t)$, plus changes in stress due to the radiation-damping effect (the second term on the right-hand side) and the transfer of stress from other places on the fault (the third term on the right-hand side). The radiation-damping effect is both the instantaneous and the long-wavelength response of a fault to slip; it expresses the stress change carried by two plane shear waves emitted, one in each direction, by the fault when it slides at velocity *V*. If the entire fault slides at the same velocity, then $\phi(x, t) = 0$ and the stress change is entirely accounted for by the radiation-damping response. This picture provides an extremely crude estimate of the conditions near the center of an expanding rupture, once the crack tips are far away. However, spatially inhomogeneous slip at other locations on the fault causes $\phi(x, t)$ to be nonzero.

[39] *Zheng and Rice* [1998] have shown that for a mode III crack-like rupture in an essentially unbounded body, slip transfers stress outside the rupture in such a way that the net force (minus any applied loads) acting on the locked portion of the fault can only be increased; that is,

$$\int_{S-S_{\text{rupt}}(t)} [\tau(x, t) - \tau_0(x, t)]dx \geq 0, \qquad (22)$$

in which *S* is the total fault area and $S_{\text{rupt}}(t)$ is the slipping area of the fault within the crack-like rupture. They also showed that no matter how the contribution to stress represented by $\phi(x, t)$ may be redistributed by waves, the net force associated with $\phi(x, t)$ acting on *S* always vanishes:

$$\int_S \phi(x, t)dx = 0. \qquad (23)$$

Combining equations (21), (22), and (23) yields

$$\int_{S_{\text{rupt}}(t)} \left[\tau(x, t) - \tau_0(x, t) + \frac{\mu}{2c_s}V(x, t)\right]dx \leq 0. \qquad (24)$$

In our work, we consider faults on which $\tau_0(x, t)$ is equal to a uniform background stress, τ^{b}, except within a small nucleation region. It follows that if $S_{\text{rupt}}(t)$ is much larger than the nucleation zone, then we can replace $\tau_0(x, t)$ in equation (24) with τ^{b}.

[40] Next, we need an approximation to the friction law. At locations within the rupture far removed from the crack tips, it is reasonable to assume, for many types of friction laws, that sufficient slip has occurred that the friction coefficient has effectively evolved to steady state conditions:

$$\tau(x, t) \approx \tau_{ss}[V(x, t)], \qquad (25)$$

The steady state conditions described by equation (25) are achieved if the timescale characterizing the evolution of slip
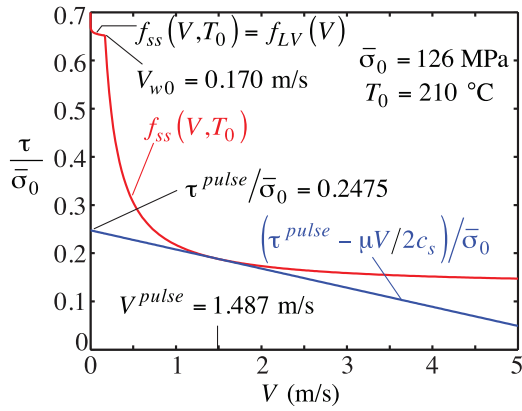
Figure 1. Steady state frictional shear stress τ_{ss} normalized by initial effective normal stress $\overline{\sigma}_0$ as a function of slip velocity V. τ^{pulse} is defined for the initial ambient conditions at 7-km depth ($T = 210°C$, $\sigma = 196$ MPa, $p = 70$ MPa) by the radiation-damping line, which fits tangentially to $\tau_{ss}(V)$ at $V = V^{pulse}$ (=1.487 m/s). The weakening slip rate is $V_w = 0.170$ m/s. Due to extreme velocity weakening at elevated slip rates, τ^{pulse} is very small (0.2475 $\overline{\sigma}_0$).

rate, $V/\dot{V}$, is much longer than the one for state evolution, L/V [*Rice and Tse*, 1986]:

$$\left| \frac{L\dot{V}}{V^2} \right| \ll 1. \tag{26}$$

The validity of this approximation is discussed further in Appendix A. Combining equations (24) and (25) and replacing $\tau_0(x, t)$ with the constant τ^b yields an integral inequality condition for the existence of crack-like ruptures. It follows that a sufficient condition for the nonexistence of crack-like ruptures is

$$\tau^b - \frac{\mu}{2c_s}V < \tau_{ss}(V) \text{ for all } V > 0. \tag{27}$$

[41] For a given material, friction law, and effective normal stress level, the only free parameter is the background stress level, τ^b. The maximum value of τ^b for which (27) holds is defined as τ^{pulse} [*Zheng and Rice*, 1998]. At stresses below τ^{pulse}, ruptures, if they exist, must assume the form of slip pulses. Laboratory experiments have confirmed that ruptures on understressed faults do take the form of slip pulses [*Lykotrafitis et al.*, 2006].

[42] Figure 1 shows the steady state friction coefficient for our flash heating model as a function of V using the initial values of T and p (and hence $\overline{\sigma}$), as well as the radiation-damping line that defines τ^{pulse}. Note that $\tau^{pulse}/\overline{\sigma}_0$ depends on initial effective normal stress, $\overline{\sigma}_0$. For $\overline{\sigma}_0 = 126$ MPa, $\tau^{pulse}/\overline{\sigma}_0$ is very small (0.2475) due to the extreme velocity weakening behavior at elevated slip rates. Note also that $\tau^{pulse}/\overline{\sigma}_0$ increases with decreasing $\overline{\sigma}_0$ since the slope of a radiation-damping line increases when normalized by $\overline{\sigma}_0$. It is interesting that *Hickman and Zoback* [2004] have noted a decrease in the value of $\tau/\overline{\sigma}$ resolved onto planes parallel to the SAF with increasing depth in the SAFOD pilot hole.

[43] For extremely low values of $\overline{\sigma}_0$ (around a few MPa), there exists a radiation-damping line which fits tangentially to $f_{ss}(V, T_0)$ in the low velocity ($V < V_w$) regime and has an intercept at $V = 0$ at a value of $\tau/\overline{\sigma}_0$ comparable to typical static friction coefficients. We do not explore the importance of this in the present study. Rather, instead of assuming that the value of pore pressure is sufficiently high to decrease the effective normal stress to these extremely low values, we consider faults that are stressed at levels far below the levels associated with steady sliding at slow slip rates.

[44] A difficulty arises when we attempt to directly apply the theory developed by *Zheng and Rice* [1998] to our models that include thermal pressurization. In fact, their theory breaks down whenever there is a set of state variables, **q**, (in our case, temperature and pore pressure) which do not have a steady state that is a function of V only, or whose characteristic displacements necessary to achieve steady state conditions are not small compared to the typical slip in an event. In such cases, the concept of a steady state is valid only for state variables other than **q**, and steady state strength must be written as

$$\tau_{ss} = \tau_{ss}(V, \mathbf{q}) \tag{28}$$

Then, the generalization of equation (27), which is the condition for the nonexistence of crack-like solutions, is

$$\tau_{ss}(V, \mathbf{q}) - \left(\tau^b - \frac{\mu}{2c_s}V \right) > 0 \text{ for all } V > 0. \tag{29}$$

Let us define τ^{pulse} using the initial value of **q**, $\mathbf{q}_0$, and assume that the evolution of **q** from its initial state weakens the fault, as will be the case for increases in p and/or T. This yields

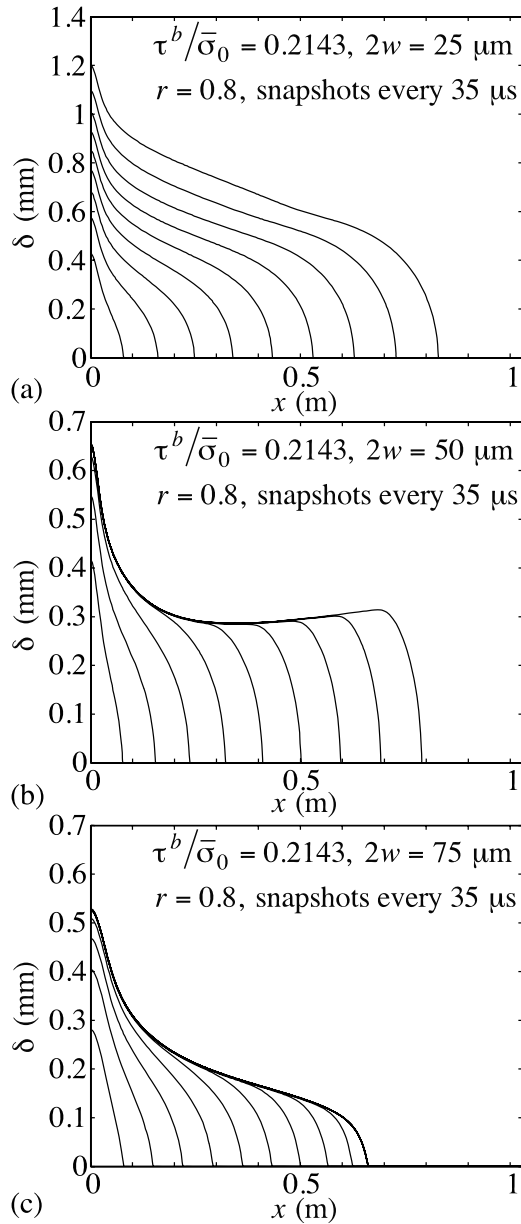$$\tau_{ss}(V, \mathbf{q}) - \left(\tau^b - \frac{\mu}{2c_s}V \right) = [\tau_{ss}(V, \mathbf{q}) - \tau_{ss}(V, \mathbf{q}_0)]$$
$$+ \left[\tau_{ss}(V, \mathbf{q}_0) - \left(\tau^b - \frac{\mu}{2c_s}V \right) \right]$$
$$> 0 \text{ for all } V > 0. \tag{30}$$

While the second bracketed term is positive for all $V \geq 0$ if $\tau^b < \tau^{pulse}$, the first bracketed term is always negative. Hence we need to evaluate the characteristic value of **q** to predict the threshold value of τ^b in this context. This is discussed later. Our numerical simulations do reveal that, following an artificial nucleation, ruptures can assume the form of cracks, growing slip pulses, and arresting slip pulses, as shown in Figure 2, and that there is an abrupt transition between the rupture modes as certain parameters (e.g., τ^b, $2w$, or α_{HT}) are varied.

[45] To assess whether or not crack-like solutions can exist, we must determine appropriate values of **q** to use in equation (30). For our model, the variables that comprise **q** are T and p on the fault. The transition to a slip pulse rupture mode occurs first in the hypocentral region, so it is necessary to estimate characteristic values of T and p there. To do so, we must first discuss our nucleation procedure.

2.4. Nucleation Procedure

[46] The extreme velocity weakening associated with flash heating makes τ^{pulse} very low (see Figure 1), and we

Figure 2. Slip distributions for (a) a growing crack, (b) a growing slip pulse, and (c) an arresting slip pulse.

explosion on the simulated fault; this lowers $\overline{\sigma}$ locally to initiate slip [*Lykotrafitis et al.*, 2006].

[47] In this work, we employ a similar, artificial nucleation procedure by applying a sudden perturbation in shear stress at the center of the fault. We caution that this is not likely to be a realistic description of the nucleation of earthquakes on natural faults. At $t = 0^-$, we set $\tau_0(x, 0^-) = \tau^b$. We also set $\Theta(x, 0) = 0.59211$, which is determined so that the friction coefficient at the rupture front is comparable to a typical static friction coefficient of 0.85. Our estimate of the peak friction coefficient at the rupture front is obtained by assuming that state evolution is negligible and that τ responds only by the direct effect.
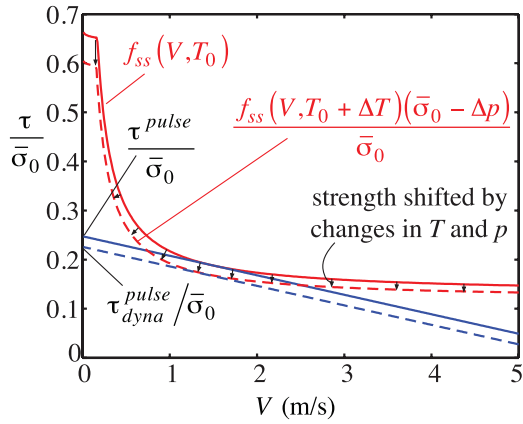
[48] At $t = 0$, we apply a Gaussian-shaped stress perturbation, the amplitude and standard deviation of which are τ^{per} and D^{per}, respectively. We use $D^{per} = 2.5$ cm and a value of τ^{per} that satisfies $\tau_0(0, 0^+) = \tau^b + \tau^{per} = 107.458$ MPa unless otherwise noted (see Table 1). This amplitude is chosen so that $V(0, 0^+)$ is 1 m/s. Weakening due to flash heating occurs immediately in the nucleation zone since $V > V_w$ there, which drives the rupture out at a speed near the shear wave speed. We would like to concentrate on the mathematical criterion between crack-like and self-healing pulse solutions, and implementing a more realistic nucleation process is beyond the scope of this work. Because of limitations in numerical resources and calculation time, it is difficult to simulate faults that are even tens of meters long, so we typically simulate ruptures propagating just over 2 m in each direction (though we do extend a few select cases out to 16 m in each direction). While these short distances are insufficient for fully examining the thermal pressurization process, the rupture mode (crack or pulse) is established over these distances with the parameters selected above.

2.5. Predicted Background Stress Levels Separating Pulses and Cracks (Variable T and p)

[49] Now that we have described our nucleation procedure, we can return to our task of estimating characteristic values of T and p, which we need to evaluate equation (30). T and p change in response to thermal pressurization driven by shear heating. Our approach is to estimate V and τ (and hence the shear heating rate) within the nucleation zone and then calculate ΔT and Δp, the changes in T and p that result from this amount of shear heating over the duration of the nucleation process. A precise description of how we estimate these changes is given in Appendix B.

[50] For each set of simulation parameters, we calculate ΔT and Δp and use these values to shift the steady state strength curve as shown in Figure 3. We define τ_{dyna}^{pulse} as the value of τ^{pulse} for these dynamic conditions; since ΔT and Δp are functions of such parameters as the shear zone width, background shear stress, and hydrothermal properties, then τ_{dyna}^{pulse} also depends on these parameters. There are no crack-like solutions for $\tau^b < \tau_{dyna}^{pulse}$, so the equality $\tau^b = \tau_{dyna}^{pulse}$ delimits the actual boundary between crack-like and pulse-like solutions.

[51] In order for a crack-like solution to exist, it is necessary for equation (24) to be satisfied. At the beginning of rupture propagation, all calculations show crack-like behavior in the sense that the center of the ruptured area is slipping, which is consistent with the locally high τ_0 within

focus on faults with background shear stresses, τ^b, near τ^{pulse}. To nucleate ruptures on faults with overall (i.e., average) stress levels that are much smaller than those associated with static friction coefficients of 0.6–0.8, either the frictional constitutive parameters or the initial stress level must be quite different on some portion of the fault. Under such circumstances, ruptures that are nucleated in one of these regions can propagate into low-stressed regions [*Perrin et al.*, 1995; *Zheng and Rice*, 1998; *Bizzarri et al.*, 2001]. Another possibility is that rupture could nucleate on a fault having a different orientation than the main fault (e.g., a branch on which the ratio of $\tau/\overline{\sigma}$ is close to the static friction level) and subsequently jump onto the main fault plane on which τ is close to τ^{pulse}. In the laboratory setting, ruptures can be nucleated on understressed faults by an

Figure 3. $\tau_{\text{dyna}}{}^{\text{pulse}}$ was defined in a similar way to *Zheng and Rice* [1998] after taking into account changes in T and p due to thermal pressurization during the nucleation process. Steady state strength is decreased due to an increase in T, which decreases $V_w(T)$ and hence $f_{ss}(V, T)$, and an increase in p, which decreases $\bar{\sigma}$.

the nucleation region. However, at later times when the rupture has propagated further, the average value of τ_0 becomes closer to τ^b and, if τ^b is too small to satisfy equation (27) or equation (30), the rupture can no longer be crack-like.

3. Rupture Mode Phase Diagrams

3.1. Neglecting Changes of T and p

[52] Before proceeding to more complicated cases, we first consider ruptures on faults where T and p are constrained to their initial values, so that strength is solely a function of V and the analysis of *Zheng and Rice* [1998] applies directly. Note that T is the macroscopic temperature on the fault, not that at the asperity contacts; hence, neglecting changes in T does not mean that we are neglecting flash heating. The upper inset of Figure 4a shows the rupture mode as a function of background stress, indicating that, as expected, there are no crack-like solutions at stresses below $\tau^{\text{pulse}} = 0.2475 \, \bar{\sigma}_0$. Ruptures take the form of growing slip pulses in a rather narrow region of τ^b around τ^{pulse}. For the cases with $\tau^b \geq 0.2778 \, \bar{\sigma}_0$, the transition to a slip pulse rupture mode does not occur during the duration of the calculation. A detailed analysis of the transition to a slip pulse rupture mode is presented in Appendix C.

3.2. Sensitivity to Width of Shear Zone

[53] Figure 4a shows a phase diagram of the rupture propagation mode in a (τ^b, $2w$) plane for $r = 0.8$. It should be emphasized that we obtain crack-like solutions for stress levels below τ^{pulse}, which is the theoretical threshold below which crack-like solutions are impossible in the absence of temperature and pore pressure changes [*Zheng and Rice*, 1998]. As the background shear stress decreases, ruptures change from expanding cracks (Figure 2a) to growing pulses (Figure 2b). For even smaller values of τ^b, ruptures are arrested (Figure 2c). There are clear boundaries between

these solution types. It is also notable that the range of background shear stress levels admitting crack-like solutions is wider for smaller $2w$, implying that thermal pressurization of pore fluid (which is more effective for narrower shear zones) extends the crack-like solution regime. As $2w$ increases, the boundary between crack-like and pulse-like solutions becomes less dependent on $2w$, but the effect of T and p changes are still remarkable in an absolute sense, compared with the case in which they are neglected.

3.3. Sensitivity to Hydraulic Properties

[54] Figure 4b shows a phase diagram of the rupture mode as a function of τ^b and the damage index r (or, equivalently, α_{HT}) with $2w = 100 \, \mu\text{m}$. We again obtain crack-like solutions below τ^{pulse}, and the phase diagram shows that changes in T and p make crack-like solutions more likely; the range of background shear stress levels permitting crack-like solutions is wider for smaller r or α_{HT}. The effect of varying hydraulic properties (within what we feel to be a realistic range) is almost as large as the effect of varying the width of the shear zone.

[55] Note that the cases in which T and p changes are neglected cannot be plotted on this section of parameter space. When the change in p is neglected with $\Lambda = 0$, T increases very rapidly and easily reaches T_w. Our constitutive model is not appropriate at such high temperatures.

3.4. Sensitivity to Nucleation

[56] The criterion for determining the rupture mode when T and p changes are permitted (i.e., our estimation of $\tau_{\text{dyna}}^{\text{pulse}}$) depends on the nucleation parameters. Here we investigate the two nucleation parameters separately. All calculations are performed with $r = 0.8$ and $2w = 100 \, \mu\text{m}$. Figures 5a and 5b show phase diagrams in the (τ^b, D^{per}) plane with fixed $\tau^b + \tau^{\text{per}} = 107.4579$ MPa, and in the (τ^b, $\tau^b + \tau^{\text{per}}$) plane with fixed $D^{\text{per}} = 2.5$ cm, respectively. The rupture mode indeed depends on the size of perturbation, with large perturbations (either in length and/or amplitude) favoring crack-like ruptures. Note that while our estimation of $\tau_{\text{dyna}}^{\text{pulse}}$ gives the right trend in the crack-pulse phase boundary, it does not precisely trace the boundary. This is presumably due to several overly simplifying approximations used to estimate the changes in p and T during the nucleation process; these are discussed in more detail in Appendix B.

4. Observational Constraints

[57] In the previous sections, we have established that ruptures on faults governed by flash heating and thermal pressurization can take the form of either slip pulses or cracks, and we have determined the conditions that give rise to each particular rupture mode. Since the crack-to-pulse transition occurs rapidly in our simulations, it was only necessary to propagate ruptures out to a few meters. However, much longer propagation distances are required to ascertain certain rupture characteristics that can be compared to observations. In particular, we are interested in addressing issues raised at the start of this manuscript regarding heat flow and the stress state around major faults. Additionally, our model makes predictions regarding
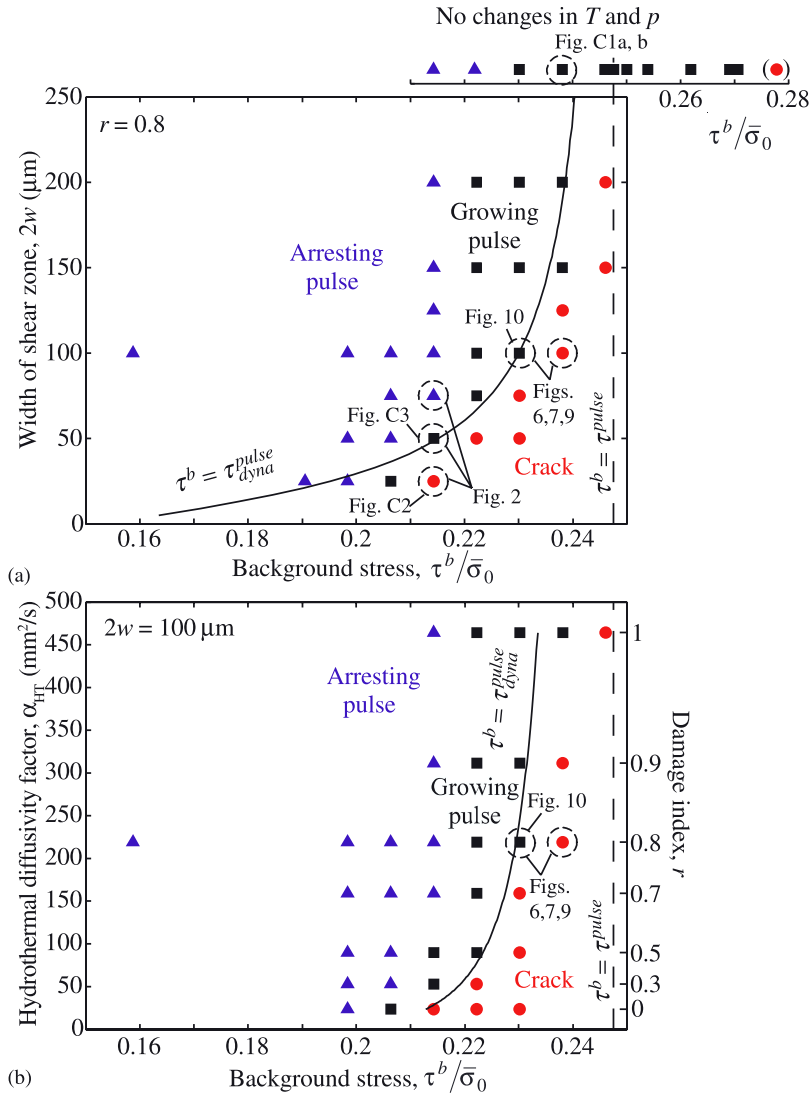
Figure 4. Phase diagrams for (a) various $2w$ with fixed r and (b) various r and fixed $2w$ for mode III rupture propagation with $L = 20$ μm, $D^{per} = 2.5$ cm, $\tau^b + \tau^{per} = 107.458$ MPa, $\Theta_0 = 0.59211$. Red circles, black squares, and blue triangles indicate crack-like, growing pulse-like, and arresting pulse-like ruptures, respectively. There are crack-like ruptures below τ^{pulse}, as defined with the initial values of T and p. When $\tau^b \leq \tau_{dyna}^{pulse}$ ruptures can only take the form of slip pulses. A one-dimensional phase diagram for the case in which T and p changes are neglected is also indicated in Figure 4a.

observables like stress drop and the scaling of slip with rupture length. To probe these questions, we have conducted two long simulations, one for a crack-like rupture and the other for a growing slip pulse, in which propagation is permitted out to 16 m in each direction; the parameters are marked in Figure 4 by "Figures 6, 7, 9". The 16 m distance is the limit of our current computational resources, and our ruptures correspond to magnitude ∼1 earthquakes (to the extent that propagation distance in our two-dimensional models can be mapped onto radius for a rupture in three dimensions). Source properties for earthquakes of this size have been studied using borehole seismograms [e.g., *Abercrombie*, 1995], and *Yamada et al.* [2005] have performed finite fault slip inversions of several mining-induced earthquakes with magnitudes between 0.8 and 1.4.

4.1. Weakening Process and Implied Slip-Weakening Relationship

[58] Our model incorporates several weakening mechanisms, and we wish to discuss here how these mechanisms act in concert during the rupture process to alter fault strength. Figure 6 shows the reduction of fault strength as a function of slip at $x = 8$ m for our two long simulations, and Figure 7 shows the history of τ, V, T, and p at this same location.

[59] The rapid rise of stress from τ^b to a peak stress of $\tau \sim$ 100 MPa ($\tau/\overline{\sigma} \sim 0.85$) is associated with the direct effect of rate-and-state friction; during this time, state evolution is negligible. As state begins to evolve, f plummets toward f_w since V is already well above V_w. By $\delta \sim 0.1$ mm, this evolution process is complete and f has essentially reached
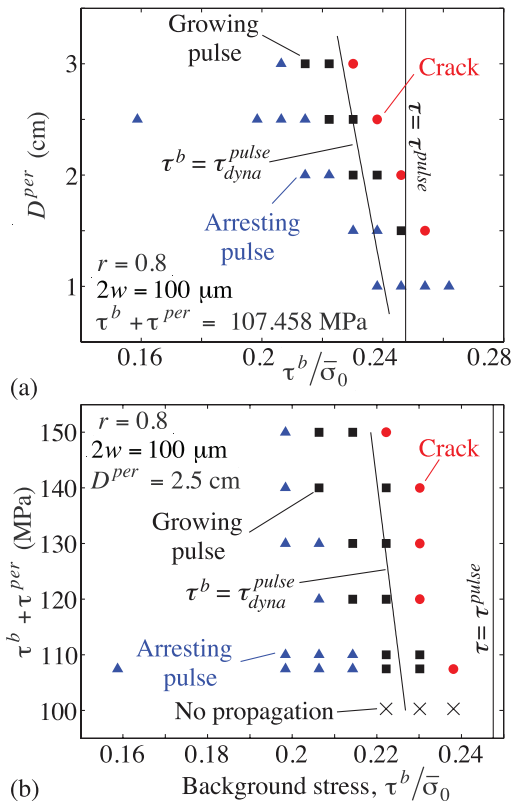
Figure 5. Phase diagrams with varying (a) length and (b) amplitude of the perturbation added to nucleate rupture.

its steady state value. Thermal pressurization is responsible for subsequent weakening. Initially the response is effectively that of undrained, adiabatic deformation; diffusion only becomes significant when the hydraulic or thermal diffusion lengths exceed the width of the shear zone (i.e., $\sqrt{4\alpha t} > w$). This occurs after about 0.2 ms (for $\alpha = 3$ mm^2/s

and $w = 50$ μm); the corresponding value of slip at this time for the ruptures shown in Figure 7 is about 1 mm. The total duration of slip for the slip pulse is about 0.15 ms at this point, so diffusion is only just becoming significant when the trailing edge of the slip pulse passes this point. This is illustrated in panels (c) and (d) of Figure 7, which show both the actual histories of ΔT and Δp in the simulations and the histories that would have resulted in the absence of thermal and hydraulic diffusion for the same shear heating histories (the latter are shown as dashed lines marked "undrained, adiabatic").

[60] The peak slip velocity is very high ($\sim$300 m/s) at the rupture tip, but values of V above 100 m/s only persist for about 1 μs. These high slip velocities imply fault-parallel strains of order 0.1 (estimated as $(V/2)/v_r$ by assuming steady state propagation at a rupture speed v_r close to c_s). Such high strains are incompatible with the assumption of a linear elastic rheology; inelastic deformation would presumably result and limit slip velocities to more reasonable values. The large stresses at the rupture front would also damage the fault walls, enhancing the ability of high pressure fluids to escape the shear zone. We approximate this by using, in some of our simulations, hydraulic properties consistent with damage-induced increases in permeability and matrix compressibility.

[61] While the strength drop associated with these ruptures is large ($\sim$90 MPa), the static stress drop (i.e., the difference between τ^b and the final stress after the event) for the slip pulse is about 3 MPa at this point. This is due to the combination of a low background stress level and the increase of stress that occurs when the fault ceases to slide. The latter is caused by an immediate return of f to its unweakened value in the absence of flash heating and a more gradual decrease of p as high pressure fluids diffuse away from the shear zone. A stress drop of 3 MPa is quite consistent with seismic data. Typical values are around 1–10 MPa (with much variation [e.g., *Kanamori and Anderson*, 1975]). *Abercrombie* [1995] and *Ide and Beroza* [1997] have shown that there is no systematic variation of
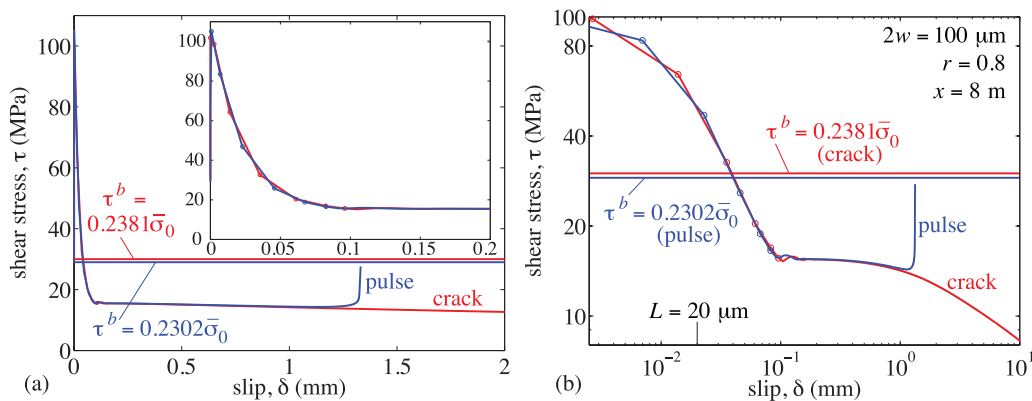
Figure 6. Implied slip-weakening curves at $x = 8$ m for a crack and a growing slip pulse shown on (a) a linear scale (with inset showing early weakening) and (b) a log-log scale. The circles correspond to the first few time steps during the weakening process. The initial weakening, during which f drops to nearly $f_w = 0.13$, is complete by $\sim$0.1 mm. Subsequent weakening is due to thermal pressurization; initially, the response is effectively undrained and adiabatic, although diffusion of heat and pore fluid becomes significant midway through the duration of slip for the slip pulse (see Figure 7).
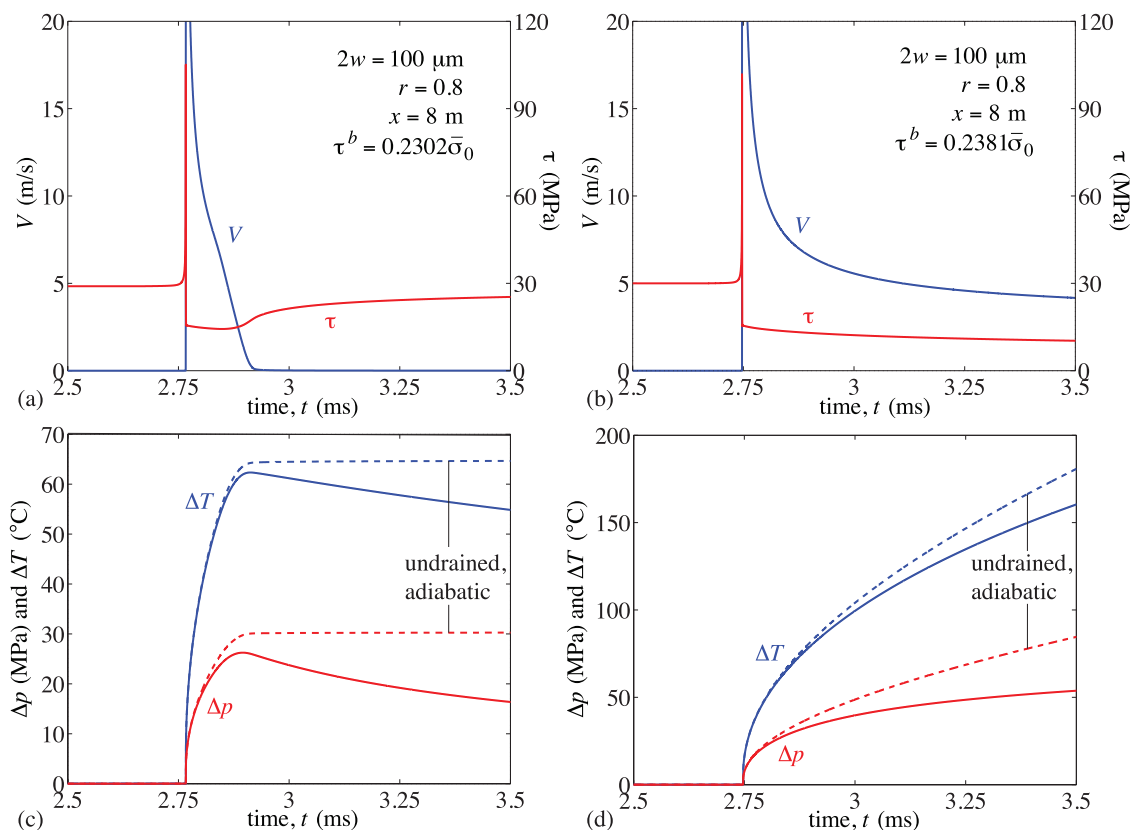
Figure 7. Time history of slip velocity and shear stress for a growing (a) slip pulse and (b) crack at $x =$ 8 m and history of temperature and pressure on the fault for the (c) slip pulse and (d) crack. The dashed lines in Figures 7c and 7d marked "undrained, adiabatic" are the T and p histories on the fault that would have resulted in the absence of thermal and hydraulic diffusion, for the same shear heating history experienced by the actual ruptures. For the first several mm of slip, the actual T and p response follows these curves closely.

average static stress drop over ten orders of magnitude in seismic moment.

[62] The fracture energy associated with the ruptures shown in Figure 6 is about 0.2 kJ/m^2. This value is quite comparable to seismic inferences of fracture energy for earthquakes with slip of ~1 mm [*Abercrombie and Rice*, 2005, Figure 8] although the form of the stress versus slip curve (rising at the end for the slip pulse) violates some of the approximations used in that study (e.g., that τ during sliding was approximately equal to the final stress after the event).

[63] The fact that stress returns nearly to τ^b after the passage of a slip pulse suggests that only a small amount of additional loading is necessary for the fault to host another rupture (as opposed to what would happen if stress drop were complete). Paleoseismic investigations by *Weldon et al.* [2004] along the SAF at Wrightwood reveal that periods of high accumulated strain are followed by either a single large earthquake or a series of relatively large (with meters of surface displacement) and frequent events separated by intervals of about 60 years. These observations suggest that after a modest static stress drop caused by a rupture, the fault is still relatively close to having the ability to rupture again.

[64] The spatial pattern of static stress drop is also interesting. Close to the nucleation region, there is little drop in stress; in fact, stress increases in the immediate vicinity of the hypocenter. This increase is characteristic of self-similar slip pulses (which have a logarithmic singularity in stress at the hypocenter), as discussed by *Nielsen and Madariaga* [2003]; and suggests that, in the absence of other sources of heterogeneity, the hypocentral region would be the most likely spot for subsequent events to nucleate.

4.2. Statically Strong, Dynamically Weak Faults

[65] As discussed in the introduction, dynamic weakening mechanisms provide one possible explanation for the absence of measurable heat flow and the low stress levels inferred to be acting on major faults. The strong rate dependence of friction predicts that the background stress level on faults should be around τ^{pulse}, far lower than the prediction of Byerlee's law. Nonetheless, the peak stress at the rupture tip exceeds 100 MPa and values of $\tau/\bar{\sigma}$ there are ~0.85, within the range of laboratory measurements of static friction (the latter being determined by our choice of the initial state Θ_0). Once nucleated, ruptures are driven by the stress concentration at their tips.
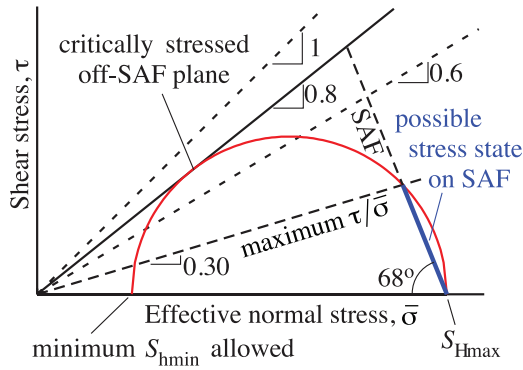
Figure 8. Stress state near the San Andreas fault (SAF) based on *Townend and Zoback* [2004], who reported the angle between S_{Hmax} and the strike of SAF as $68 \pm 7°$. The minimum S_{hmin} allowed is determined by the strength of a fracture in the optimal orientation. The estimate of the maximum $\tau/\overline{\sigma}$ is 0.30, close to both the directly measured value of 0.24 at the bottom of the SAFOD pilot hole at 2.1-km depth [*Hickman and Zoback*, 2004] and what our simulations show is the minimum stress necessary to propagate ruptures.

[66] The average stress doing work (i.e., producing heat) during slip at some point on the fault is

$$\tau^{heat}(x) = \frac{\int_0^\infty \tau(x,t)V(x,t)dt}{\int_0^\infty V(x,t)dt}. \qquad (31)$$

τ^{heat} drops monotonically from about 22 MPa at $x = 1$ m to slightly less than 15 MPa by $x = 15$ m; the decrease with propagation distance is a consequence of the fact that weakening due to thermal pressurization becomes more effective as slip accumulates. Our simulations, which are limited in terms of propagation distance (and thus the magnitude of pressure changes from thermal pressurization), strongly suggest that τ^{heat} for large events will be well below the upper bound of ~10 MPa that heat flow measurements place on τ^{heat} [*Brune et al.*, 1969; *Lachenbruch and Sass*, 1980; *Lachenbruch et al.*, 1995; *Williams et al.*, 2004].

[67] We can also interpret the stress state around major faults like the SAF in light of our model. *Townend and Zoback* [2004] report that the regional direction of maximum horizontal compression, S_{Hmax}, in central and southern California is $68 \pm 7°$ as measured from the local strike of the SAF. Assuming that $\tau/\overline{\sigma}$ within the crust is bounded by typical static friction levels (0.6–0.9), as is observed at many locations [*Townend and Zoback*, 2000], we can constrain the maximum value of $\tau/\overline{\sigma}$ on planes parallel to the SAF (Figure 8). For an angle of 68° between the fault and S_{Hmax} and a static friction coefficient of 0.8, $\tau/\overline{\sigma} < 0.30$ on the SAF. Direct measurement of stresses in the SAFOD pilot hall [*Hickman and Zoback*, 2004] reveal that $\tau/\overline{\sigma}$ on the SAF decreases with depth from 0.6 at about 1.2 km depth to 0.24 at the bottom of the pilot hole at 2.1 km depth. Furthermore, a number of geodynamic studies find values for the long-term average stress supported by major faults in the range of $\tau/\overline{\sigma} \approx 0.2$–0.3 [*Bird and Kong*, 1994; *Humphreys and Coblentz*, 2007]. These low values of $\tau/\overline{\sigma}$

are exactly what our model predicts, without any alteration of hydrothermal and frictional properties from their laboratory-measured values.

4.3. Scaling of Slip and Slip Pulse Length With Propagation Distance

[68] Over the modeled propagation distance of 16 m, our ruptures appear to be growing in an approximately self-similar manner. In particular, the total slip locked in by the slip pulse increases nearly linearly with propagation distance, as shown in Figure 9a. Figure 9b shows the slip history of the crack-like rupture, with that of the slip pulse overlaid for comparison. Slip at the center of the crack-like rupture increases at about 1 mm/m rupture length. When a crack-like rupture terminates, stopping phases propagate inward to lock the fault; during this time, additional slip occurs, such that the final displacement at the center could be nearly twice as large as the instantaneous value shown here. Then the average final slip in the area ruptured in a crack-like event will be on the order of 1 mm/m rupture length. On the other hand, for a growing slip pulse, the final slip grows with distance from the center at about 0.14 mm/m (Figure 9a). Assuming this M-shaped linear slip profile persists as the rupture grows, the average slip per rupture length is 0.07 mm/m, which is in good agreement with measurements of 0.01–0.1 mm/m for large earthquakes [*Scholz*, 1982; *Scholz et al.*, 1986; *Manighetti et al.*, 2005].

[69] Another indication of self-similar growth is that, after an initial transient related to the nucleation process and the transition to a slip pulse rupture mode, the length of the slip pulse increases linearly with time. By assuming a rupture speed of c_s (as is seen in our simulations), we can convert time into propagation distance; see Figure 10, which shows the length of the slip pulse in Figure 9a as a function of propagation distance. We used the condition $V > V_{th}$ for threshold velocities ranging from $V_{th} = 0.001$–0.1 m/s to define the extent of the actively slipping region. Regardless of the value of V_{th}, the length of the slip pulse grows at a rate of about 30 m/km, which is in acceptable agreement with, though about three times smaller than, lengths based on risetimes inferred from slip inversions of large events compiled by *Heaton* [1990], though those measurements are limited in their resolution by the finite bandwidth of seismic data. Multiple time window slip inversions of magnitude ~1 mining-induced earthquakes, which have source dimensions of 10–20 m, suggest risetimes around 3–4 ms (much larger than risetimes in our simulations; see Figure 7a), though these values are likely upper bounds since the width of the time windows used was 1.5 ms [*Yamada et al.*, 2005].

[70] The rate at which the slip pulse length increases with propagation distance can be related to the relative speed of the rupture front, v_r, and the healing front, v_h. The rate of 30 m/km = 0.03 is equal to, at least for large times, $(v_r t - v_h t)/(v_r t) = 1 - v_h/v_r$, implying that $v_h = 0.97 v_r$. The self-similar slip pulse solutions of *Nielsen and Madariaga* [2003] and *Broberg* [1999, p. 418] have the following property: Given a value of G, the energy supplied to the crack tip per unit area advance of the crack, relative to G_0, the value of G for a quasi-statically expanding crack of the same length, there is a unique relationship between v_r and v_h. The very low values of G in our simulations (a consequence of small L) require that v_r be close to the limit speed c_s.
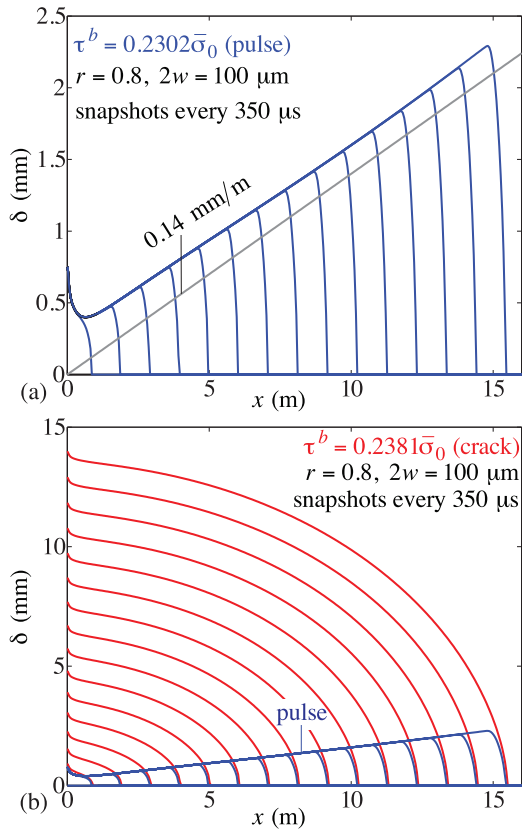
Figure 9. Snapshots of slip on the fault for a growing (a) slip pulse and (b) crack. While the background stress level for the two ruptures differs by only 1 MPa, the crack exhibits over an order of magnitude more slip than the slip pulse. The linear increase of slip with distance (at a rate of ∼0.14 mm/m = 0.14 m/km) for the slip pulse is consistent with geological measurements.

However, in this limit, small variations in v_r at fixed G/G_0 are associated with large variations in v_h, making it difficult to constrain expected values of v_h. Exactly what determines the precise value of v_r (and hence v_h) in our simulations remains unclear. In particular, we caution that the measured rate of increase of slip and pulse length with propagation distance may be sensitive to the artificial nucleation process we employ. This issue requires further study.

5. Summary

[71] The thermal weakening mechanisms of flash heating of microscopic asperities and thermal pressurization of pore fluid have been implemented into a spectral boundary integral equation code for elastodynamic rupture propagation. Flash heating is encapsulated in a framework of rate-and-state friction that includes the direct effect and evolution toward steady state conditions over a slip distance L. We use values of L comparable to asperity dimensions (∼20 μm), as suggested by laboratory experiments, and a range of hydrothermal properties consistent with laboratory measurements of fault gouge and reasonable assumptions about the degree of damage induced by the passage of high stress concentrations near rupture fronts.

[72] For faults with a purely velocity-weakening steady state strength, *Zheng and Rice* [1998] have shown the existence of a critical stress level, τ^{pulse}, below which crack-like ruptures cannot exist. The value of $\tau^{\text{pulse}}/\bar{\sigma}$ predicted by the observed velocity dependence of flash heating is about 0.2–0.3. We have generalized the theory of *Zheng and Rice* [1998] to accommodate weakening mechanisms that involve a set of variables (like T and p in our model) that do not achieve velocity-dependent steady states over the duration of a rupture. When temperature and pore pressure are permitted to evolve in response to shear heating, theoretical considerations and a series of calculations reveal that additional weakening due to thermal pressurization enables ruptures to propagate in the crack-like rupture mode at background stresses slightly below τ^{pulse}. However, while thermal pressurization mildly increases the range of crack-like solutions in parameter space, it does not prevent the occurrence of self-healing slip pulses. While there is only minor sensitivity of the crack-pulse phase boundary to the thermal pressurization parameters, the efficiency of thermal pressurization is likely to be important in determining the average stress doing work within ruptures at larger amounts of slip than those we have been able to model in this work. Furthermore, we have found that temperature and pressure conditions within the shear zone are quite sensitive to its width, even for widths below 100 μm.

[73] Our models suggest that faults will host ruptures at the minimum stress level required for a rupture, once nucleated, to propagate in a self-sustaining manner. This critical level is around $\tau^{\text{pulse}}/\bar{\sigma} \sim 0.2$–$0.3$, which is consistent with the stress state inferred to be acting on major faults like the SAF. At this critical stress level, ruptures take the
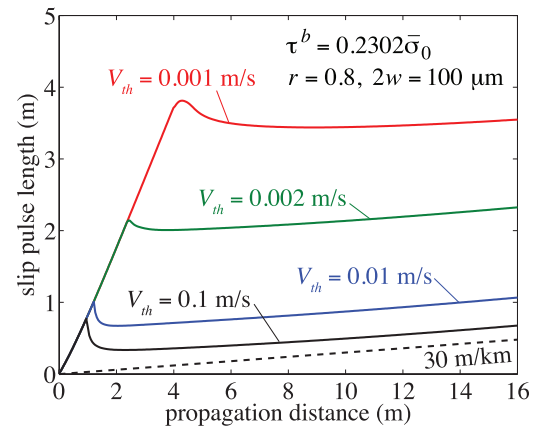
Figure 10. Slip pulse length (or half of the extent of the actively slipping region, prior to slip arrest at the hypocenter) as a function of propagation distance for the rupture shown in Figure 9a. The slip pulse is defined by the condition $V > V_{\text{th}}$ (for various threshold velocities V_{th}) and propagation distance is taken to be the product of rupture speed (assumed to be c_s) and time since nucleation. The initial transient is related to nucleation and the transition to a slip pulse rupture mode. While the length of the slip pulse depends on the chosen value of V_{th}, the rate at which pulse length increases with propagation distance, after the initial transient, is about 30 m/km for all V_{th}.

form of slip pulses. Such slip pulses have reasonable static stress drops of ~3 MPa and expand in a nearly self-similar manner, such that slip increases with propagation distance at a rate of ~0.14 mm/m. The average stress doing work during slip, τ^{heat}, is below 15 MPa, and this quantity is expected to decrease with increasing propagation distance since thermal pressurization will have more time to reduce fault strength.

[74] We have chosen to use parameter values taken directly from laboratory experiments, which constrains us to model two-dimensional ruptures out to only 16 m in each direction from the hypocenter, extrapolating our results to larger source dimensions. An outstanding question we have not addressed is how different the ground motion generated by our ruptures might be from those using more common parameter values. For example, most rupture models (like those in the Southern California Earthquake Center code validation tests [*Harris and Archuleta*, 2004; *Harris et al.*, 2009]) feature strength drops that are only ~10 MPa larger than static stress drops; in our simulations, the strength drop is around ~90 MPa.

Appendix A: Justification of Steady State Strength Assumption

[75] In deriving the condition for the nonexistence of crack-like ruptures, *Zheng and Rice* [1998] made the assumption that the fault strength had evolved to its steady state value, i.e., $\tau(x, t) \approx \tau_{ss}[V(x, t)]$. We can justify this assumption further by considering the slip history of a self-similarly expanding singular crack with constant stress drop $\Delta\tau$:

$$\delta(x,t) = F\left(\frac{v_r}{c_s}\right)\frac{\Delta\tau}{\mu}\sqrt{(v_rt)^2-x^2}, \tag{A1}$$

where δ is slip on the fault, v_r is rupture velocity, and $F(v_r/c_s)$ is close to unity [*Kostrov*, 1964; *Nielsen and Madariaga*, 2003]. The associated slip velocity history is

$$V(x,t) = F\left(\frac{v_r}{c_s}\right)\frac{\Delta\tau}{\mu}\frac{v_r}{\sqrt{1 - (x/v_rt)^2}}. \tag{A2}$$

The assumption of a constant stress drop may be valid if the friction coefficient at elevated slip rates is only modestly dependent on V, as in our flash heating model for $V \gg V_w$.

[76] For this singular crack model, the condition given by equation (26), i.e., that the timescale characterizing the evolution of slip rate is much longer than the one for state evolution, becomes

$$\left|\frac{L\dot{V}}{V^2}\right| = \frac{1}{F(v_r/c_s)}\frac{\mu}{\Delta\tau}\frac{L}{\sqrt{(v_rt)^2-x^2}}\left(\frac{x}{v_rt}\right)^2 \ll 1. \tag{A3}$$

Because $1/F(v_r/c_s)$ and $x/(v_r t)$ are of order unity or smaller, this becomes

$$\frac{\mu}{\Delta\tau}L \ll \sqrt{(v_rt)^2-x^2} \tag{A4}$$

Near the crack tip, where $x = v_r t - R$ for $R \ll v_r t$, $x^2 \approx (v_r t)^2 - 2\,v_r tR$ and equation (A3) becomes

$$R \gg \frac{L^2}{2v_rt}\left(\frac{\mu}{\Delta\tau}\right)^2. \tag{A5}$$

This predicts that the region where the approximation $\tau \approx \tau_{ss}(V)$ does not hold vanishes as $t \to \infty$. For $L = 10$ μm, $\Delta\tau = 3$ MPa, and $v_r t = 5$ m, this gives $R \gg 1$ mm.

Appendix B: Characteristic Changes in T and p During Nucleation

[77] In this appendix, we estimate characteristic changes in T and p during the nucleation process. We seek only an estimate here and will consequently employ several approximations. Our approach is to estimate V and τ (and hence the shear heating rate) within the nucleation zone and then calculate the changes in T and p that result from this amount of shear heating over the duration of the nucleation process.

[78] Using the Gaussian shape for our stress perturbation leads to a complicated evolution of V and τ within the nucleation zone. To simplify things, we consider instead an equivalent boxcar-shaped perturbation of amplitude τ^p and half-width D^p. These parameters are related to τ^{per} and D^{per} by setting $D^p = 3\,D^{per}$ (so that 99.7% of the Gaussian-shaped perturbation lies within the boxcar-shaped perturbation) and preserving the net force imparted by the perturbation. It follows that $\tau^p = 0.42\,\tau^{per}$. The characteristic duration of the nucleation process is taken to be the time it takes a shear wave to cross the boxcar perturbation, i.e., $2\,D^p/c_s = 6\,D^{per}/c_s$. For $D^{per} = 2.5$ cm, this is 50 μs.

[79] We further assume that when the perturbation is applied at $t = 0$, f drops instantaneously to f_w. This is justified if the resulting V far exceeds V_w and the state evolution time is small compared to the duration of the nucleation process. Assuming small changes in p, the fault strength is then $\tau = f_w\,\bar{\sigma}_0$. For a spatially uniform stress field, the elastodynamic response is the radiation-damping response; for an applied load of $\tau^b + \tau^p$ within the boxcar perturbation, that suggests $\tau \approx \tau^b + \tau^p - (\mu V)/(2c_s)$. Setting stress equal to strength and eliminating τ^p in favor of τ^{per}, we find $V \approx 2\,c_s(\tau^b + 0.42\,\tau^{per} - f_w\,\bar{\sigma}_0)/\mu$. Typical values of V are ~10 m/s, so $V \gg V_w$. At this V, slipping a distance of $L = 20$ μm takes only ~2 μs, which is far less than the characteristic duration of nucleation.

[80] Now that we have estimated characteristic values of τ and V during the nucleation process, we can estimate changes in T and p. As discussed by *Andrews* [2002] and *Rice* [2006], the solution to equations (11) and (12) for an arbitrary shear heating history $\omega(z, t)$ can be written as

$$T(z,t) = T_0 + \frac{1}{\rho c}\int_0^t\int_{-\infty}^{\infty}\omega(z',t')g(z-z',t-t';\alpha_{th})dz'dt' \tag{B1}$$

$$p(z,t) = p_0 + \frac{\Lambda}{\rho c}\int_0^t\int_{-\infty}^{\infty}\omega(z',t')$$
$$\cdot\frac{\alpha_{hy}g(z-z',t-t';\alpha_{hy}) - \alpha_{th}g(z-z',t-t';\alpha_{th})}{\alpha_{hy} - \alpha_{th}}dz'dt', \tag{B2}$$

in which the Green's function for the diffusion equation is

$$g(z, t; \alpha) = \frac{1}{2\sqrt{\pi \alpha t}} \exp\left(-\frac{z^2}{4\alpha t}\right) H(t) \qquad \text{(B3)}$$

and $H(t)$ is the unit step function. *Andrews* [2002] has evaluated the spatial convolutions in equations (B1) and (B2) for a Gaussian shear zone, for which $\omega(z, t)$ is given by equation (13).

[81] The expressions further simplify if we consider a heat source that turns on abruptly at $t = 0$ and remains constant thereafter. Both τ and V (and hence the shear heating rate) will be approximately constant within the boxcar-shaped perturbation over the duration of the nucleation process. In this case, the solution to equations (B1) and (B2) on the fault (i.e., at $z = 0$) for $t \geq 0$ is

$$\Delta T(t) = T(0, t) - T_0$$
$$= \frac{\tau V}{\sqrt{2\pi}\rho c} \frac{\sqrt{4\alpha_{th} t + w^2} - w}{\alpha_{th}} \qquad \text{(B4)}$$

$$\Delta p(t) = p(0, t) - p_0$$
$$= \Lambda \frac{\tau V}{\sqrt{2\pi}\rho c} \frac{\sqrt{4\alpha_{hy} t + w^2} - \sqrt{4\alpha_{th} t + w^2}}{\alpha_{hy} - \alpha_{th}}. \qquad \text{(B5)}$$

Thus using the above expressions we can estimate characteristic changes in T and p from their initial values for each set of simulation parameters. This method works well for estimating the sensitivity of the crack-pulse phase boundary to hydraulic properties and the width of the shear zone, as evidenced by Figure 4. The approximation of a Gaussian-shaped perturbation by a boxcar-shaped one means that we neglect stress transfer between adjacent points within the nucleation zone, and this is not always well justified over the entire range of perturbation amplitudes and widths explored in Figure 5. As a consequence, our formula for τ_{dyna}^{pulse} should be considered an estimate rather than a precise result; an improved treatment of the elastodynamic response would presumably improve this.

Appendix C: Details of the Crack-Pulse Transition

C1. Transition Behavior Neglecting T and p Changes

[82] As explained previously, *Zheng and Rice* [1998] derived a critical background shear stress below which crack-like ruptures are impossible, and they also provided a criterion that helps determine the solution type at higher stress levels (where both crack-like and pulse-like ruptures are possible). If (and only if) $\tau^b \geq \tau^{pulse}$, there exists a value of velocity, V_*, defined as the maximum value of V for which $\tau^b - (\mu V)/(2 c_s) = \tau_{ss}(V)$, which we can use to define a nondimensional parameter,

$$T_{ZR} = -\frac{\partial \tau_{ss}/\partial V}{\mu/(2c_s)}\bigg|_{V=V_*}. \qquad \text{(C1)}$$

If T_{ZR} is near unity, then the solution is pulse like. Our calculations show, however, that even a case with $T_{ZR} = 0.1758$ ($\tau^b/\overline{\sigma}_0 = 0.2706$) yields a slip pulse solution.

[83] Figure C1a shows the evolution of (V, f) at $x = 0.1$ m for the pulse-like rupture indicated in Figure 4a as "Figure C1a." Figure C1b presents a magnified view of the transition to the slip pulse rupture mode. $f_{ss}(V, T_0)$ and a radiation-damping line which fits tangentially to $f_{ss}(V, T_0)$ are also plotted. [1] to [4] in these figures mark the following sequence of events. As the rupture front approaches, the fault is loaded with almost no state evolution because V is very small [1]. At the rupture front, f achieves its maximum value. Behind the rupture front, state evolution and unloading (corresponding to a decrease in ϕ) lower f slightly below $f_{ss}(V, T_0)$ [2]. As the fault decelerates, f follows a path nearly parallel to $f_{ss}(V, T_0)$ [3]. When V reaches V^{pulse}, defined as the slip rate where $f_{ss}(V, T_0)$ and a radiation-damping line intersect tangentially (Figure 1), f departs from a path parallel to $f_{ss}(V, T_0)$ and moves onto a trajectory that approximately follows the radiation-damping line that is just tangent to $f_{ss}(V, T_0)$ [4]. This transition is similar to one reported by *Cochard and Madariaga* [1994] although V dropped to zero abruptly in their case due to the use of a purely rate-dependent friction law.

[84] Figure C1c shows slip rate histories at $x = 0.1$ m for different values of $\tau^b/\overline{\sigma}_0$. The horizontal line represents V^{pulse}, where the transition to a pulse-like solution occurs. With increasing $\tau^b/\overline{\sigma}_0$, the transition time increases monotonically. Note that in the case with $\tau^b/\overline{\sigma}_0 = 0.2778$, the transition does not occur during the duration of the calculation but V keeps decreasing. Here the question arises, is this solution incorrectly identified as crack-like simply because the calculation is too short? Figure C1d is a plot of the inverse of the crack-pulse transition time as a function of $\tau^b/\overline{\sigma}_0$, which reveals that the transition time appears to diverge at a finite value of $\tau^b/\overline{\sigma}_0$ around 0.28. Therefore we conclude that there are indeed crack-like solutions that will never become pulses, no matter how far they propagate.

C2. Transition Behavior Accounting for T and p Changes

[85] When T and p are permitted to change, certain properties of the crack-like solutions also change. Figure C2a shows the evolution of slip rate for the crack-like rupture shown in Figure 2a ($r = 0.8$, $2w = 25$ μm, $\tau^b/\overline{\sigma}_0 = 0.2143$). Deceleration of fault motion takes place behind the rupture front followed later by acceleration. We take this acceleration as an indication of the transition to a crack-like solution. The calculations with T and p changes were carried out at least until we recognized the transition to a crack-like solution or growing/arresting slip pulse solution. Figure C2b shows a plot of friction coefficient versus slip rate at $x = 0.1$ m. The trajectory traces in the direction of decreasing V just below $f_{ss}(V, T)$ behind the rupture tip although $f_{ss}(V, T)$ depends on T. However, at a certain point, the trajectory reverses and moves in the direction of higher velocities and lower friction coefficients. In this case, V, T, and p keep increasing (Figure C2c), and it is likely that this point will eventually achieve either a complete stress drop or the onset of melting; its fate depends on hydraulic properties and the width of the shear zone [*Rempel and Rice*, 2006]. Figure C2d shows the history of f and $f_{ss}(V, T)$ at $x = 0.1$ m, indicating that
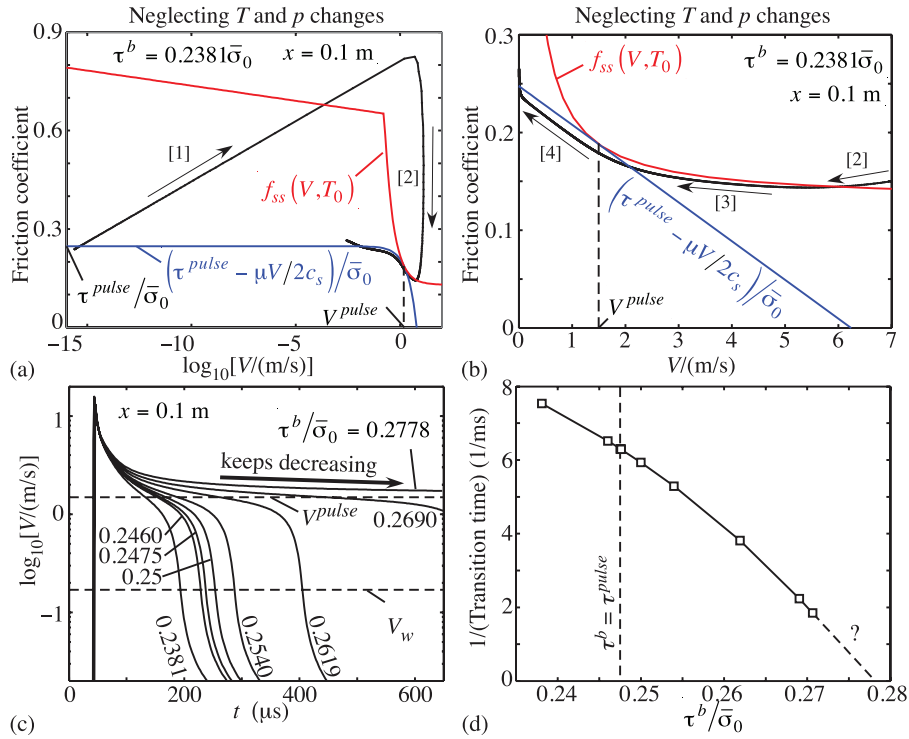
Figure C1. (a) A trajectory of (V, f) for a pulse-like solution, neglecting changes in T and p, at $x = 0.1$ m. Parameters are indicated in Figure 2. The transition to a pulse-like solution is recognized by the deviation from $\tau_{ss}(V) = \overline{\sigma}_0 f_{ss}(V, T_0)$ at $V = V^{pulse}$. (b) The trajectory around the transition to pulses plotted in a linear velocity scale. [1] to [4] correspond to the stages of the fault motion explained in the text. (c) Slip rate histories for various τ^b. The transition time to a pulse-like solution increases with τ^b, and for the case with $\tau^b/\overline{\sigma}_0 = 0.2778$, the transition does not occur during the calculation. (d) Inverse of the transition time plotted against τ^b, showing that the transition time diverges at a finite τ^b.

$f_{ss}(V, T)$ becomes larger than f at the transition to a crack-like solution and, after that, f traces just above $f_{ss}(V, T)$.

[86] Figure C3a shows details of the growing pulse solution in Figure 4b ($r = 0.8$, $2w = 50$ μm, $\tau^b/\overline{\sigma}_0 = 0.2143$). This case is very similar to the case without T and p changes; behind the rupture front, f traces just below $f_{ss}(V, T)$ before changing its track to a radiation-damping line (Figure C3b). Figure C3c shows the history of V, T, and p at $x = 0.1$ m, showing how diffusion of heat and fluid away from the shear zone reduce T and p after fault motion ceases; this is accompanied by an increase in fault strength. In pulse-like solutions, f is always below $f_{ss}(V, T)$ after the rupture front passes, and the transition to a pulse-like solution takes place before one to a crack-like solution (Figure C3d). Following the discussion in the previous sections, we discuss this in terms of V^{pulse}.

C3. Improved Condition for Nonexistence of Crack-like Ruptures

[87] We can also use the singular crack model discussed in Appendix A to obtain an improved estimate of the critical stress level below which crack-like ruptures cannot exist. Our strategy is to estimate the elastodynamic relation between τ and V from the singular crack solution, and ask whether or not there is a simultaneous solution to this equation and the steady state strength expression (equation 25).

[88] At $x = 0$, the slip rate in the singular crack solution is

$$V_\infty = F\left(\frac{v_r}{c_s}\right)\frac{\Delta\tau}{\mu}v_r, \tag{C2}$$

and, at $x \neq 0$, slip rate decreases from infinity at the rupture front to V_∞ as $t \to \infty$. If $V_\infty > V^{pulse}$, then rupture likely continues in a crack-like mode. On the other hand, if $V_\infty < V^{pulse}$, then rupture will transition to pulse-like mode. Therefore a condition for a pulse-like rupture can be written as

$$F\left(\frac{v_r}{c_s}\right)\frac{\Delta\tau}{\mu}\frac{v_r}{V^{pulse}} < 1. \tag{C3}$$

With the current selection of the parameters, $V^{pulse} = 1.487$ m/s, at which $f_{ss}(V^{pulse}, T_0) = 0.1885$. Approximating $(v_r/c_s)F(v_r/c_s) \approx 1$, equation (C3) yields $\Delta\tau < 14.87$ MPa, or $\Delta\tau/\overline{\sigma}_0 < 0.1180$. The friction coefficient at high slip rates is between $f_{ss}(V^{pulse}, T_0)$ and f_w, the average of which is $f_d = 0.1593$. Then the condition on τ^b for a pulse-like rupture is

$$\frac{\tau^b}{\overline{\sigma}_0} = f_d + \frac{\Delta\tau}{\overline{\sigma}_0} < 0.2773, \tag{C4}$$

which agrees well with the background stress level at which the transition time diverges, although there is uncertainty in estimating $\Delta\tau$ and v_r.
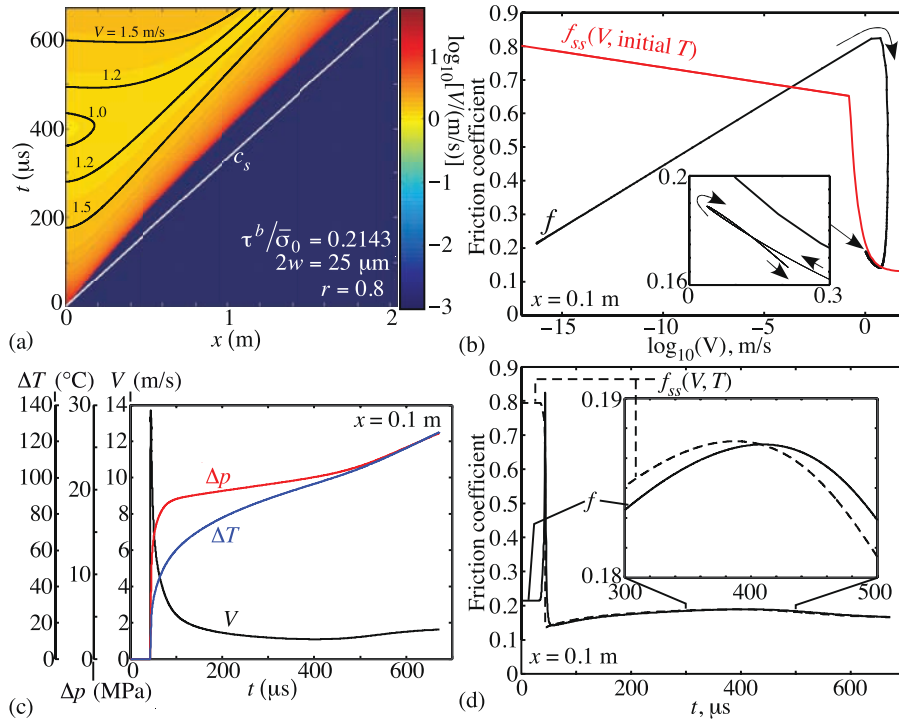
Figure C2. A crack-like solution accounting for changes in T and p due to shear heating. (a) Evolution of V. Slip acceleration occurs in the central region of the rupture. The white lines show contours for $V = 1.0$, 1.2, and 1.5 m/s. Contours at the rupture tip are not plotted. (b) A trajectory of (V, f) at $x = 0.1$ m reverses in the high-V and low-f direction (indicating the transition to a crack-like solution). (c) Time history of V, T, and p at $x = 0.1$ m. T and p keep increasing after the transition to a crack-like solution. (d) Time history of f and $f_{ss}(V, T)$. At the transition to a crack-like solution, f becomes larger than $f_{ss}(V, T)$.

Appendix D: Numerical Implementation

[89] In this appendix, we describe the implementation of thermal pressurization and flash heating (in the framework of rate-and-state friction) in our spectral boundary integral equation code. We first discretize the fault using a uniform grid spacing Δx (in the boundary integral equation method, only the fault is discretized). Diffusion of heat and pore fluid is calculated using a finite difference method by setting, at each point along the fault, a one-dimensional grid perpendicular to the fault with uniform spacing Δz. This is illustrated in Figure D1a.

[90] At each point on the fault, the system of equations that we solve, specifically equations (1), (8), (11), (12), and (21), can be written in the form

$$\frac{\partial \delta}{\partial t} = V(x,t) \qquad (D1)$$

$$\frac{\partial \theta_i}{\partial t} = G_i\big[V(x,t), \{\theta_j(x,t)\}\big] \quad (i,j = 1, 2, \ldots), \qquad (D2)$$

with $V(x, t)$ given by the functional equation obtained by equating the elastic shear stress to the interfacial shear strength (i.e., by combining equations (1) and (21)):

$$\tau_0(x,t) - \frac{\mu}{2c_s}V(x,t) + \phi(x,t) = \overline{\sigma}f[V(x,t), \{\theta_i(x,t)\}]. \qquad (D3)$$

Here $\{\theta_i(x, t)\}$ contains both the state variable Θ and the set of values of T and p after spatial discretization of the diffusion equations in the z direction. G_i denotes a known function describing the temporal evolution of $\theta_i(x, t)$ (i.e., the state evolution equation and the spatially discretized thermal pressurization equations). The functional term $\phi(x, t)$ is a convolution of the slip history with a known elastodynamic kernel $K(x, t)$:

$$\phi(x,t) = \int_0^t \int_{-\infty}^{\infty} K(x - x', t - t')\delta(x', t')dx'dt'. \qquad (D4)$$

The convolution is performed by representing $\delta(x, t)$, and hence $\phi(x, t)$, as a function which is periodic in x with repeat length λ that is chosen large enough so that waves from neighboring replicates do not influence rupture development over the time of calculation. Hence $\delta(x, t)$ and $\phi(x, t)$ can be written as Fourier series in x, which we truncate to the finite series

$$\delta(x,t) = \sum_{n=-N/2}^{N/2} D_n(t) \exp(2\pi i n x/\lambda)$$

$$\phi(x,t) = \sum_{n=-N/2}^{N/2} F_n(t) \exp(2\pi i n x/\lambda), \qquad (D5)$$

where N is a large even number and, because the functions δ and ϕ are real, D_{-n} and F_{-n} are the respective complex
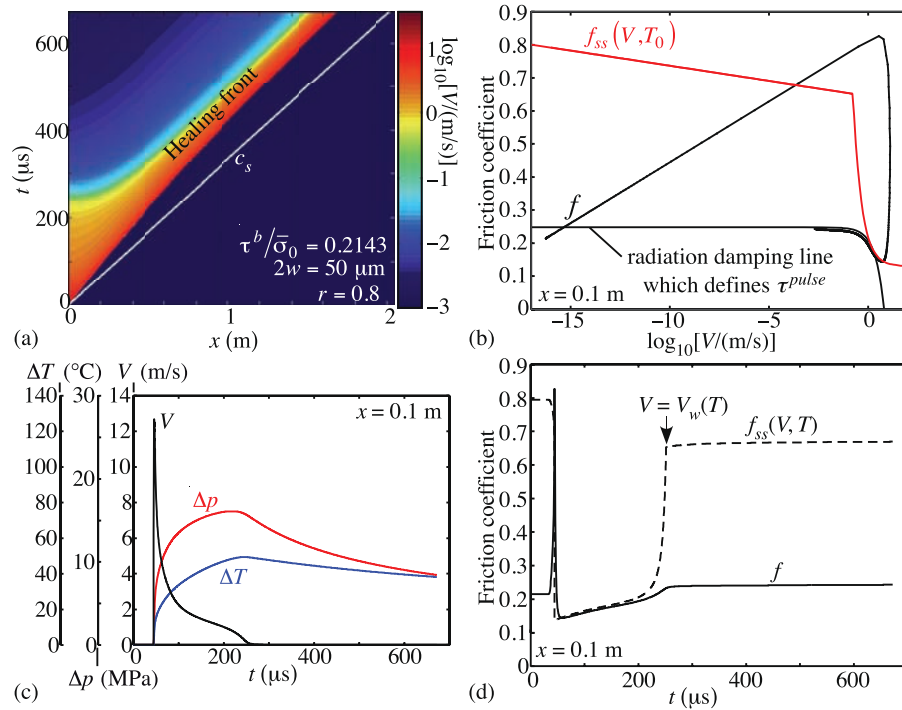
Figure C3. A growing slip pulse solution accounting for changes in T and p due to shear heating. (a) Evolution of V. Healing of the fault is initiated at the central region and propagates at slightly less than c_s. (b) A trajectory of (V, f) at $x = 0.1$ m changes its track from $f_{ss}(V, T)$ to a radiation-damping line at the transition to a pulse-like solution. (c) Time history of V, T, and p at $x = 0.1$ m. T and p decrease because of diffusion after the fault is locked. (d) Time history of f and $f_{ss}(V, T)$ at $x = 0.1$ m. The transition to a slip pulse solution occurs (f diverges from $f_{ss}(V, T)$) before the transition to a crack-like solution occurs.

conjugates of D_n and F_n (and D_0 and F_0 are real). The convolution is then equivalent to

$$F_n(t) = \int_0^t \hat{K}(2\pi n/\lambda, t - t')D_n(t')dt'$$

$$\hat{K}(k, t) = \int_{-\infty}^{\infty} K(x, t) \exp(-ikx)dx. \tag{D6}$$

For mode III ruptures $\hat{K}(k, t) = -(\mu|k|/2) J_1(|k|c_s t)/t$, where J_1 is a Bessel function [*Perrin et al.*, 1995].

[91] In keeping with FFT methodology, we represent the coefficients D_n, F_n in terms of the values of δ, ϕ at N equally spaced spatial sample points $x_k = k\,\lambda/N$, with $k = 0, 1, 2, \ldots, N - 1$ (in the actual calculation, we shift x_k by $-\lambda/2$ to place the center of our rupture at $x = 0$). The imaginary parts of $D_{N/2}$, $F_{N/2}$ correspond to coefficients of the term $\sin(\pi N x/\lambda)$ in the Fourier series, which vanishes at all the sample points. Those coefficients, like all the neglected ones of higher frequency ($|n| > N/2$) sine and cosine terms in a complete series, cannot be determined by the N sample point values, and are set to zero (i.e., we require that $D_{N/2}$, $F_{N/2}$ be real). Then, for example, in the case of δ and D_n, with notation $\delta_k(t) = \delta(x_k, t)$,

$$\delta_k(t) = \sum_{n=-N/2}^{N/2} D_n(t) \exp(2\pi i n k/N) \tag{D7}$$

and multiplication by $\exp(-2\pi\,imk/N)$ and summing on k from 0 to $N - 1$ shows the inverse expression

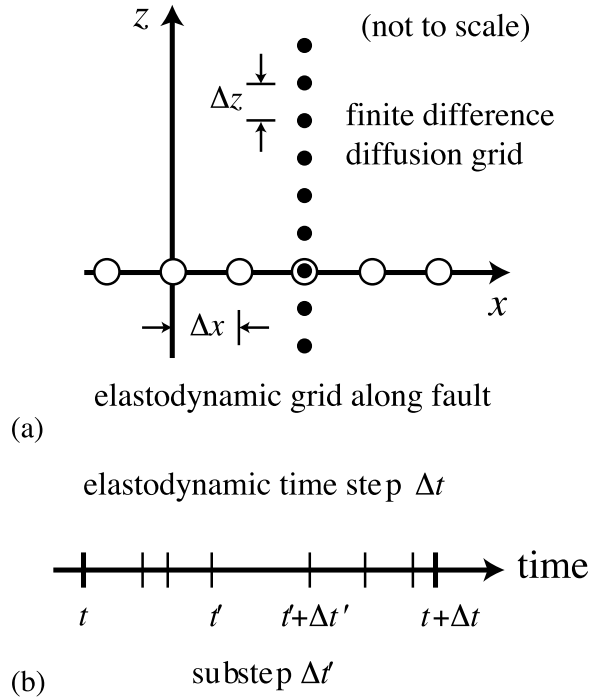$$D_m(t) = \frac{1}{N} \sum_{k=0}^{N-1} \delta_k(t) \exp(-2\pi imk/N),$$

$$m = 0, 1, 2, , \frac{N}{2} - 1$$

$$D_{N/2}(t) = \frac{1}{2N} \sum_{k=0}^{N-1} \delta_k(t) \exp[-2\pi i(N/2)k/N]. \tag{D8}$$

Note that D_0 and $D_{N/2}$ are thus given as real expressions (the exp terms are then ± 1) so there is the expected number, $2 + 2 \times (N/2 - 1) = N$, of parameters in this representation. For further discussion of this representation, see *Trefethen* [2000, pp. 17–19]. Standard FFT routines can be used to go back and forth, as we must do in each time step, from spatial (δ_k) to spectral (D_n) representations.

[92] The initial conditions $\delta(x, 0)$ and $\{\theta_i(x, 0)\}$ are given. Note that neither $\tau(x, 0)$ nor $V(x, 0)$ can be specified independently of the given initial conditions; instead, they are calculated by solving the constraint equation (D3). Combining equations (D1)–(D4) yields a set of coupled functional differential equations for $\delta(x, t)$ and $\{\theta_i(x, t)\}$.

[93] An extensive literature exists on the numerical solution of functional differential equations [e.g., *Baker*, 1996, 2000; *Brunner*, 2004]. Solution methods are similar to those for ordinary differential equations (ODE), with the additional necessity of choosing an appropriate quadrature rule

z

Δz

(not to scale)

finite difference
diffusion grid

Δx

x

elastodynamic grid along fault

(a)

elastodynamic time step Δt

time

t t' $t'+\Delta t'$ $t+\Delta t$

(b) substep $\Delta t'$

Figure D1. Schematic diagrams showing discretization (a) in space and (b) in time. (a) Heat and fluid flow are solved on a one-dimensional finite difference grid perpendicular to the fault, and (b) multiple substeps are taken adaptively within a single elastodynamic time step.

to evaluate the functional term $F_n(t)$. With the exception of certain low order quadrature methods, this requires a continuous approximation of $D_n(t)$ for any past time t. The main classes of ODE solvers, such as one-step (e.g., Runge-Kutta [*Enright et al.*, 1994]) and multistep methods, can be brought to bear on functional differential equations [*Tavernini*, 1971; *Cryer and Tavernini*, 1972]. The particular approach we use in this study is a second-order method similar to Heun's method [*Cryer and Tavernini*, 1972] and the method proposed by *Lapusta et al.* [2000] within the context of the spectral boundary integral equation elastodynamic framework. The method can be thought of as a second-order predictor-corrector method, for which higher-order generalizations in the form of multistep methods have been studied by *Jackeiwicz* [1986]. The method falls within the class of continuous Runge-Kutta methods [*Baker*, 1996; *Bellen and Zennaro*, 2003] which permit evaluation of $D_n(t')$ (and $\{\theta_i(x, t')\}$, though this is not necessary) for any t' in $[0, t]$ (which permits the use of high-order quadrature rules to evaluate the functional term). The second-order method we use provides second-order accurate values of $D_n(t')$ via a quadratic interpolation polynomial, as discussed by *Bellen and Zennaro* [2003, p. 122] and *Maset et al.* [2005]. For those wishing to develop higher order one-step methods, *Maset et al.* [2005] has introduced a family of explicit continuous Runge-Kutta methods up to fourth order. For neutral functional differential equations (i.e., ones in which the time derivative of the field appears within the functional term), an approximation to the rates at past times is also needed and an iterative solution for the rates at the current time step

is required [*Enright and Hu*, 1997]. This case arises for our equations if the functional in (D4) is integrated by parts to extract the static elastic response. The remaining convolution integral involves the spatial Fourier transform of $V(x,t)$ at the current and previous times [*Perrin et al.*, 1995; *Geubelle and Rice*, 1995]. *Jackeiwicz* [1986] cautions that the approximation of the rates must be at least one order greater than the approximation of the fields; otherwise, the method suffers from order reduction.

[94] The method we describe below explicitly integrates our system of equations with second-order accuracy in time, provided that the solution and its derivatives are sufficiently continuous. Heat and fluid mass transport, equations (11) and (12), are calculated using an explicit finite difference method by setting a uniformly spaced one-dimensional grid perpendicular to the fault plane (Figure D1). We assume a symmetric response of the two sides of the fault, which permits us to restrict our attention to one side only, using the boundary conditions

$$\left.\frac{\partial T}{\partial z}\right|_{z=0} = 0 \tag{D9}$$

$$\left.\frac{\partial p}{\partial z}\right|_{z=0} = 0 \tag{D10}$$

Since the integration method is explicit, the time step must be sufficiently small for stability. Insight into the time step stability constraints can be obtained by a matrix analysis of the discrete system (e.g., as done in the work of *Lapusta et al.* [2000]). We have performed this analysis by studying the stability properties of steady sliding (for which a linear temperature profile exists normal to the fault). While this analysis provided insight into the necessary time step restrictions, we ultimately adopted an adaptive time integration procedure that automatically selects the step size in order to bound error below a specified tolerance. However, it is useful to briefly comment on several easily recognized time step constraints. There are at least three timescales of interest in our equations. First, the elastodynamic timescale is the transit time of a shear wave between neighboring grid points along the fault, $\Delta x/c_s$. Second, the state variable evolves over L/V. Third, we have the diffusion timescale between neighboring grid points normal to the fault, $\Delta z^2/\alpha_{max}$, where $\alpha_{max} = \max\{\alpha_{th}, \alpha_{hy}\}$. The first two timescales are linked by the choice of Δx, and selection of a proper Δx guarantees that the elastodynamic time step is sufficient for integration of the state evolution equation as well [e.g., *Lapusta et al.*, 2000]. The diffusion timescale is somewhat independent of the first two, and for the parameters and resolutions of interest to us, it is always shorter than the other timescales. Increasing the spatial resolution of the diffusion grids while holding everything else fixed increases the difference between the diffusion and elastodynamic timescales. For the typical resolutions of interest in this work, there are typically tens of diffusion time steps within a single elastodynamic time step, making our system moderately stiff. One option would be to integrate the entire system of equations at the smallest time step; however, this requires storage of the slip history at all of these smaller time steps, which increases memory

requirements by an order of magnitude. Furthermore, evaluation of the temporal convolution is computationally expensive, so we wish to avoid this if possible. Therefore we have adopted a substepping procedure (Figure D1b), in which we integrate our system of equations over smaller time steps within a single elastodynamic time step. To do this, we store the slip history (as $D_n(t)$) and also compute $\phi(x, t)$ only at the elastodynamic time steps, but interpolate $\phi(x, t)$ when integrating within the elastodynamic time step.

[95] The specific method to advance from the current time t to $t + \Delta t$ follows. Assume that the values of $\delta(x, t)$ and $\{\theta_i(x, t)\}$ are known from the previous time step, as well as the functional term $\phi(x, t)$ and the slip history $\delta(x, t')$ for t' in $[0, t]$.

[96] 1. Set the slip rate at the beginning of the time step by setting stress equal to strength and solving, for $V(x, t)$, the nonlinear equation (D3).

[97] 2. Explicitly integrate slip:

$$\delta(x, t + \Delta t) = \delta(x, t) + \Delta t V(x, t). \quad (D11)$$

[98] 3. Evaluate the stress transfer functional $\phi(x, t + \Delta t)$ using the procedure discussed below.

[99] 4. Return to the start of the elastodynamic time step and adaptively integrate from t to $t + \Delta t$. In particular, the problem at each point on the fault is posed as a set of coupled ODEs. While the system of equations to be solved is identical to that given before in equations (D1), (D2), and (D3), instead of evaluating the computationally expensive convolution in (D4) at each substep, the functional term is now approximated by a quadratic interpolant through $\phi(x, t - \Delta t)$, $\phi(x, t)$, and $\phi(x, t + \Delta t)$:

$$\phi(x, t') = \phi(x, t) + \frac{t' - t}{2\Delta t}[\phi(x, t + \Delta t) - \phi(x, t - \Delta t)]$$
$$+ \frac{(t' - t)^2}{2\Delta t^2}[\phi(x, t + \Delta t) - 2\phi(x, t) + \phi(x, t - \Delta t)]. \quad (D12)$$

Note that this requires knowing $\phi(x, t - \Delta t)$, which we store in memory. For the first time step, we simply use a linear interpolant. Using this continuous function $\phi(x, t')$, it is possible to integrate the set of ODEs with any conventional ODE integration package. In this work, we use an embedded 3(2) Runge–Kutta procedure that bounds relative error at each substep below a given tolerance (taken to be 10^{-3} here). The particular scheme we use is given by *Dormand* [1996, p. 79], and provides both a second- and third-order estimate of the solution (the difference of which provides an estimate of the error associated with the second-order solution). We run the scheme in local extrapolation mode by updating with the higher-order estimate, despite the fact that an error estimate exists only for the lower order estimate. The adaptive time steps are determined by a PID (proportional-integral-derivative) feedback error controller that utilizes error estimates from previous time steps within a control-theoretic framework to provide smooth variations in time step lengths [*Gustafsson*, 1991; *Söderlind*, 2002; *Hairer and Wanner*, 2004]. At the end of this step, we have values of $\delta(x, t + \Delta t)$ and $\{\theta_i(x, t + \Delta t)\}$.

[100] 5. Iterate by repeating steps 3 and 4 as many times as desired to obtain increasingly more accurate values of $\delta(x, t + \Delta t)$, $\{\theta_i(x, t + \Delta t)\}$, and $\phi(x, t + \Delta t)$. A single iteration, as taken in Heun's method, is used in this work.

[101] Heun's method is an example of a continuous Runge–Kutta method for which a second-order accurate estimate of $\delta(x, t')$ for t' in $[t, t + \Delta t]$ is given by the quadratic interpolation formula (obtained by integration of a linear interpolant for $V(x, t')$ between t and $t + \Delta t$):

$$\delta(x, t') = \delta(x, t) + V(x, t)(t' - t)$$
$$+ \frac{1}{2}[-V(x, t) + V(x, t + \Delta t)]\frac{(t' - t)^2}{\Delta t}. \quad (D13)$$

A similar formula provides $\theta_i(x, t')$. Note, in particular, that

$$\delta(x, t + \Delta t) = \delta(x, t) + \frac{1}{2}[V(x, t) + V(x, t + \Delta t)]\Delta t, \quad (D14)$$

as is used in the second integration step. The estimate of δ at the midpoint of the time step, which might be used in a midpoint quadrature method for evaluating $\phi(x, t + \Delta t)$ is

$$\delta(x, t + \Delta t/2) = \delta(x, t) + \left[\frac{3}{8}V(x, t) + \frac{1}{8}V(x, t + \Delta t)\right]\Delta t \quad (D15)$$

rather than the average of the values at t and $t + \Delta t$:

$$\delta(x, t + \Delta t/2) \neq \frac{1}{2}[\delta(x, t) + \delta(x, t + \Delta t)]$$
$$= \delta(x, t) + \frac{1}{4}[V(x, t) + V(x, t + \Delta t)]\Delta t. \quad (D16)$$

To compute the transform of the functional, $F_n(t + \Delta t)$, we must define an appropriate quadrature rule for the temporal convolution. It has been shown that the order of the quadrature rule must be greater than or equal to the order of the step-advancement scheme to preserve the overall order of accuracy [*Cryer and Tavernini*, 1972]. In our method, we know (and have stored) the values of $D_n(t)$ at a set of uniformly spaced elastodynamic time steps $\{t_n\} = \{n \Delta t\}$, $n = 0, 1, \ldots$. We then integrate using the trapezoid rule, which provides a second-order accurate formula:

$$F_n(t + \Delta t) = \frac{\Delta t}{2}\hat{K}(k, t + \Delta t)D_n(0)$$
$$+ \Delta t \sum_{n=1}^{N} \hat{K}(k, t + \Delta t - t_n)D_n(t_n)$$
$$+ \frac{\Delta t}{2}\hat{K}(k, 0)D_n(t + \Delta t). \quad (D17)$$

The midpoint rule could alternatively be used, using the value given by the continuous interpolant (D15).

Appendix E: Convergence Analyses

[102] Because of extremely short state evolution distances ($L \sim 20~\mu$m), and high rates of velocity weakening, it is challenging to simulate even several meters of rupture
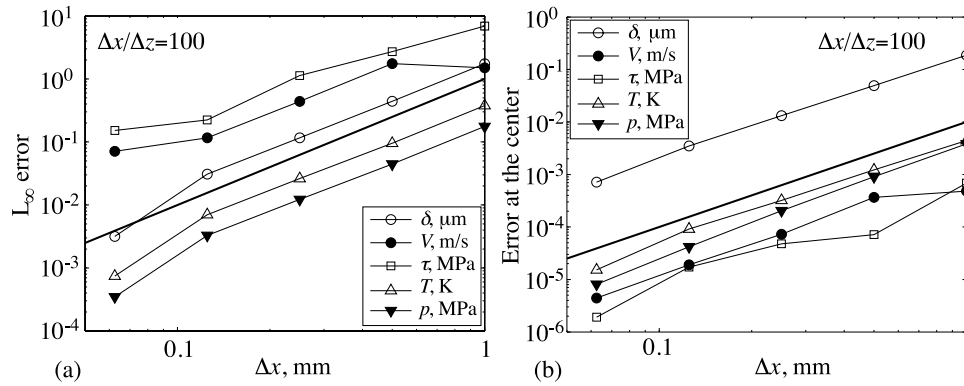
Figure E1. Convergence test performed by refining Δx and Δz with a fixed ratio of $\Delta x/\Delta z = 100$, for the case with $\tau^b/\overline{\sigma}_0 = 0.2381$ and $2w = 100$ μm at time $t = 84$ μs. The heavy black line shows second-order convergence. (a) Global L_∞ error, which is typically determined by a single point at the rupture front. (b) Error at $x = 0$, which is important in resolving the transition to crack-like or pulse-like solutions.

propagation. Neglecting thermal pressurization, the critical grid spacing required for a stable numerical solution with rate-and-state friction is [*Lapusta et al.*, 2000]

$$h_* = \frac{\pi}{4} \frac{\mu L}{\max\{-\partial f_{ss}/\partial(\ln V)\}\overline{\sigma}_0}, \quad (E1)$$

where max is taken over all V, is very small. The constitutive law, equation (6), and the physical properties used in this work (Table 1) yield $h_* = 7.003$ mm, with the maximum value of $-\partial f_{ss}/\partial(\ln V)$ occurring at $V = V_w$.

[103] h_* is obtained from a linear stability analysis about states of steady sliding. Under the highly nonlinear conditions at a rupture front, the length scale that must be resolved for an accurate solution is that characterizing the strength drop, from approximately $f_0 \overline{\sigma}_0$ to $f_w \overline{\sigma}_0$. This length scale is $\sim \mu L/(f_0 - f_w) \overline{\sigma}_0$ times a monotonically decreasing function of v_r. Contraction of the process zone with increasing v_r makes this problem even more numerically demanding than implied by equation (E1).

[104] We first conducted a set of convergence tests in which we refined either Δx or Δz while holding the other grid spacing fixed. With these tests we were able to determine the relative contribution to the total error coming from the spatial discretization of the elastodynamic equation and from the diffusion equations. To maximize computational efficiency, it is desirable that the relative error contributions be approximately equal. In other words, nothing is gained by using an incredibly fine grid spacing for the diffusion equations without simultaneously using a fine grid spacing to discretize the fault. We found that the error contributions from the two spatial discretizations were approximately equal for $\Delta x/\Delta z = 100$.

[105] We then performed a convergence test in which we refined both Δx and Δz simultaneously, with a fixed ratio of $\Delta x/\Delta z = 100$, for the case with $2w = 100$ μm, $r = 0.8$, and $\tau^b/\overline{\sigma}_0 = 0.2381$. Figure E1a shows the L_∞ errors (the maximum, over the entire fault, of the absolute value of the error) in δ, V, τ, T, and p at $t = 84$ μs, with respect to the case with $\Delta x = 3.125 \times 10^{-2}$ mm and $\Delta z = 3.125 \times 10^{-4}$ mm, showing second-order convergence. Note that the L_∞ errors are almost always determined by a single grid point at

the rupture front. The magnitude of the numerical error is not negligibly small at the rupture front; for $\Delta x = 0.5$ and 1 mm, the L_∞ error in V is on the order of 1 m/s and the peak value of V is around 15.6 m/s (making a 6% relative error). However, the main target of this work is to determine the rupture mode (crack or pulse), and the distinguishing features of these rupture modes are first seen in the central region of the rupture (Figures C2a and C3a). Figure E1b shows the error in the fields at the central pair of grid points, showing that the numerical error in V at the center of the rupture is very small, and the solution converges with second-order accuracy; with $\Delta x = 1$ mm, the error in V is below 1 mm/s. In the calculations presented in the main part of this paper, we use $\Delta x = 0.5$ mm and $\Delta z = 5$ μm in the cases with $2w = 100$ μm, such that the expected numerical errors are on the order of 0.01 μm in δ, 0.1 mm/s in V, 0.1 kPa in τ, 10^{-3} K in T, and 1 kPa in p at the center of the rupture. In simulations with different values of $2w$, we change Δz to maintain a fixed number of grid points within the shear zone by setting $\Delta z = 0.1w$.

References

Abercrombie, R. E. (1995), Earthquake source scaling relationships from -1 to 5 M_L using seismograms recorded at 2.5-km depth, *J. Geophys. Res.*, 100(B12), 24,015–24,036.

Abercrombie, R. E., and J. R. Rice (2005), Can observations of earthquake scaling constrain slip weakening?, *Geophys. J. Int.*, 162, 406–424, doi:10.1111/j.1365-246X.2005.02579.x.

Andrews, D. J. (2002), A fault constitutive relation accounting for thermal pressurization of pore fluid, *J. Geophys. Res.*, 107(B12), 2363, doi:10.1029/2002JB001942.

Andrews, D. J. (2005), Thermal pressurization explains enhanced long-period motion in the Chi-chi earthquake, *Eos Trans. AGU*, 86(52), Fall Meet. Suppl., Abstract S34A-04.

Andrews, D. J., and Y. Ben-Zion (1997), Wrinkle-like slip pulse on a fault between different materials, *J. Geophys. Res.*, 102(B1), 553–571.

Archard, J. F. (1958/1959), The temperature of rubbing surfaces, *Wear*, 2, 438–455.

Baker, C. T. H. (1996), Numerical analysis of Volterra functional and integral equations—state of the art, *Tech. Rep. 292*, Manchester Centre for Computational Mathematics, Num. Anal. Rep., Manchester, U. K.

Baker, C. T. H. (2000), A perspective on the numerical treatment of Volterra equations, *J. Comp. Appl. Math.*, *125*(1–2), 217–249.

Beeler, N. M., and T. E. Tullis (1996), Self-healing pulse in dynamic rupture models due to velocity-dependent strength, *Bull. Seismol. Soc. Am.*, *86*, 1130–1148.

Beeler, N. M., and T. E. Tullis (2003), Constitutive relationships for fault strength due to flash-heating, in *SCEC Annual Meeting Proceedings and Abstracts*, vol. XIII, p. 66, South. Calif. Earthquake Cent., Los Angeles.

Beeler, N. M., T. E. Tullis, M. L. Blanpied, and J. D. Weeks (1996), Frictional behavior of large displacement experimental faults, *J. Geophys. Res.*, *101*(B4), 8697–8715.

Beeler, N. M., T. E. Tullis, and D. L. Goldsby (2008), Constitutive relationships and physical basis of fault strength due to flash heating, *J. Geophys. Res.*, *113*, B01401, doi:10.1029/2007JB004988.

Bellen, A., and M. Zennaro (2003), *Numerical Methods for Delay Differential Equations*, Oxford Univ. Press, Oxford, U. K.

Beroza, G., and T. Mikumo (1996), Short slip duration in dynamic rupture in the presence of heterogeneous fault properties, *J. Geophys. Res.*, *101*(B10), 22,449–22,460.

Bird, P., and X. Kong (1994), Computer simulations of California tectonics confirm very low strength of major faults, *Geol. Soc. Am. Bull.*, *106*(2), 159–174.

Bizzarri, A., and M. Cocco (2006a), A thermal pressurization model for the spontaneous dynamic rupture propagation on a three-dimensional fault: 1. Methodological approach, *J. Geophys. Res.*, *111*, B05303, doi:10.1029/2005JB003862.

Bizzarri, A., and M. Cocco (2006b), A thermal pressurization model for the spontaneous dynamic rupture propagation on a three-dimensional fault: 2. Traction evolution and dynamic parameters, *J. Geophys. Res.*, *111*, B05304, doi:10.1029/2005JB003864.

Bizzarri, A., M. Cocco, D. J. Andrews, and E. Boschi (2001), Solving the dynamic rupture problem with different numberical approaches and constitutive laws, *Geophys. J. Int.*, *144*, 656–678.

Boettcher, M. S., and C. Marone (2004), Effects of normal stress variation on the strength and stability of creeping faults, *J. Geophys. Res.*, *109*, B03406, doi:10.1029/2003JB002824.

Bowden, F. P., and P. H. Thomas (1954), The surface temperature of sliding solids, *Proc. R. Soc. London A*, *223*, 29–40.

Broberg, K. B. (1999), *Cracks and Fracture*, Academic Press, London, U. K.

Brodsky, E. E., and H. Kanamori (2001), Elastohydrodynamic lubrication of faults, *J. Geophys. Res.*, *106*(B8), 16,357–16,374.

Brune, J. N., T. L. Henyey, and R. F. Roy (1969), Heat flow, stress, and rate of slip along the San Andreas Fault, California, *J. Geophys. Res.*, *74*(15), 3821–3827.

Brunner, H. (2004), *Collocation Methods for Volterra Integral and Related Functional Differential Equations*, Cambridge Univ. Press, Cambridge, U. K.

Bureau, L., T. Baumberger, and C. Caroli (2000), Shear response of a frictional interface to a normal load modulation, *Phys. Rev. E*, *62*, 6810–6820.

Burnham, C. W., J. R. Holloway, and N. F. Davis (1969), Thermodynamic properties of water to 1000°c and 10,000 bars, *Spec. Pap. Geol. Soc. Am.*, *132*, 96 pp.

Byerlee, J. (1978), Friction of rocks, *Pure Appl. Geophys.*, *116*, 615–626.

Cardwell, R. K., D. S. Chinn, G. F. Moore, and D. L. Turcotte (1978), Frictional heating on a fault zone with finite thickness, *Geophys. J. Int.*, *52*(3), 525–530.

Chester, F. M., and J. S. Chester (1998), Ultracataclasite structure and friction processes of the Punchbowl fault, San Andreas system, California, *Tectonophysics*, *295*, 199–221.

Chester, J. S., and D. L. Goldsby (2003), Microscale characterization of natural and experimental slip surfaces relevant to earthquake mechanics, *SCEC Ann. Prog. Rep.*, South. Calif. Earthquake Cent., Los Angeles.

Chester, F. M., J. S. Chester, D. L. Kirschner, S. E. Schulz, and J. P. Evans (2004), Structure of large-displacement, strike-slip fault zones in the brittle continental crust, in *Rheology and Deformation in the Lithosphere at Continental Margins*, edited by G. D. Karner et al., pp. 223–260, Columbia Univ. Press, New York.

Cocco, M., and A. Bizzarri (2004), Dynamic fault weakening caused by thermal pressurization in an earthquake model governed by rate- and state-dependent friction, *Eos Trans. AGU*, *85*(47), Fall Meet. Suppl., Abstract T22A-06.

Cochard, A., and R. Madariaga (1994), Dynamic faulting under rate-dependent friction, *Pure Appl. Geophys.*, *142*, 419–445.

Cochard, A., and R. Madariaga (1996), Complexity of seismicity due to highly rate-dependent friction, *J. Geophys. Res.*, *101*(B11), 25,321–25,336.

Cryer, C. W., and L. Tavernini (1972), The numerical solution of Volterra functional differential equations by Euler's method, *SIAM J. Numer. Anal.*, *9*(1), 105–129.

da Cruz, F., S. Emam, M. Prochnow, J. N. Roux, and F. Chevoir (2005), Rheophysics of dense granular materials: discrete simulation of plane shear flows, *Phys. Rev. E*, *72*(2), 021309, doi:10.1103/PhysRevE.72.021309.

Day, S. M. (1982), Three-dimensional finite difference simulation of fault dynamics: Rectangular faults with fixed rupture velocity, *Bull. Seismol. Soc. Am.*, *72*, 705–727.

Di Toro, G., D. L. Goldsby, and T. E. Tullis (2004), Friction falls toward zero in quartz rock as slip velocity approaches seismic rates, *Nature*, *427*, 436–439, doi:10.1038/nature02249.

Di Toro, G., T. Hirose, S. Nielsen, G. Pennacchioni, and T. Shimamoto (2006), Natural and experimental evidence of melt lubrication of faults during earthquakes, *Science*, *311*, 647–649, doi:10.1126/science.1121012.

Dieterich, J. H. (1979), Modeling of rock friction: 1. Experimental results and constitutive equations, *J. Geophys. Res.*, *84*(B5), 2161–2168.

Dormand, J. R. (1996), *Numerical Methods for Differential Equations: A Computational Approach*, 368 pp., CRC Press LLC, New York.

Enright, W. H., and M. Hu (1997), Continuous Runge-Kutta methods for neutral Volterra integro-differential equations with delay, *Appl. Numer. Math.*, *24*, 175–190.

Enright, W. H., D. J. Higham, B. Owren, and P. W. Sharp (1994), A survey of the explicit Runge-Kutta method, *Tech. Rep. TR 291/94*, Department of Computer Science, Univ. of Toronto, Toronto.

Ettles, C. M. (1986), The thermal control of friction at high sliding speeds, *J. Tribol.*, *108*, 98–104.

Faulkner, D. R., and E. H. Rutter (1998), The gas permeability of clay-bearing fault gouge at 20°C, in *Faulting, Fault Sealing and Fluid Flow in Hydrocarbon Reservoirs*, vol. 147, edited by G. Jones, Q. J. Fisher, and R. J. Knipe, pp. 147–156, Geol. Soc. London, Spec. Publ.

Faulkner, D. R., and E. H. Rutter (2000), Comparisons of water and argon permeability in natural clay-bearing fault gouges under high pressure at 20°C, *J. Geophys. Res.*, *105*(B7), 16,415–16,426.

Faulkner, D. R., and E. H. Rutter (2003), The effect of temperature, nature of the pore fluid, and sub-yield differential stress on the permeability of phyllosilicate-rich fault gouge, *J. Geophys. Res.*, *108*(B5), 2227, doi:10.1029/2001JB001581.

Fialko, Y., and Y. Khazan (2004), Fusion by earthquake fault friction: Stick or slip?, *J. Geophys. Res.*, *110*, B12407, doi:10.1029/2005JB003869.

Geubelle, P. H., and J. R. Rice (1995), A spectral method for three-dimensional elastodynamic fracture problems, *J. Mech. Phys. Solids*, *43*, 1791–1824.

Goldsby, D. L., and T. E. Tullis (2002), Low frictional strength of quartz rocks at subseismic slip rates, *Geophys. Res. Lett.*, *29*(17), 1844, doi:10.1029/2002GL015240.

Gustafsson, K. (1991), Control theoretic techniques for stepsize selection in explicit Runge–Kutta methods, *ACM Trans. Math. Soft.*, *17*(4), 533–554.

Hairer, E., and G. Wanner (2004), *Solving Ordinary Differential Equations II: Stiff and Differential-Algebraic Problems*, 3rd ed., 614 pp., Springer, Berlin.

Han, R., T. Shimamoto, T. Hirose, J.-H. Ree, and J. Ando (2007), Ultralow friction of carbonate faults caused by thermal decomposition, *Science*, *316*(5826), 878–881, doi:10.1126/science.1139763.

Hardebeck, J. L., and E. Hauksson (2001), Crustal stress field in southern california and its implications for fault mechanics, *J. Geophys. Res.*, *106*(B10), 21,859–21,882.

Hardebeck, J. L., and A. J. Michael (2004), Stress orientations at intermediate angles to the San Andreas Fault, California, *J. Geophys. Res.*, *109*, B11303, doi:10.1029/2004JB003239.

Harris, R. A., and R. J. Archuleta (2004), Seismology: Earthquake rupture dynamics: Comparing the numerical simulation methods, *Eos Trans. AGU*, *85*(34), 321, doi:10.1029/2004EO340003.

Harris, R. A., et al. (2009), The SCEC/USGS dynamic earthquake-rupture code verification exercise, *Seismol. Res. Lett.*, *80*(1), doi:10.1785/gssrl.80.1.119.

Heaton, T. H. (1990), Evidence for and implications of self-healing pulses of slip in earthquake rupture, *Phys. Earth Planet. Int.*, *64*, 1–20.

Heermance, R., Z. K. Shipton, and J. P. Evans (2003), Fault structure control on fault slip and ground motion during the 1999 rupture of the Chelungpu Fault, Taiwan, *Bull. Seismol. Soc. Am.*, *93*(3), 1034–1050.

Hickman, S., and M. Zoback (2004), Stress orientations and magnitudes in the SAFOD pilot hole, *Geophys. Res. Lett.*, *31*, L15S12, doi:10.1029/2004GL020043.

Hirose, T., and T. Shimamoto (2005), Growth of a molten zone as a mechanism of slip weakening of simulated faults in gabbro during frictional melting, *J. Geophys. Res.*, *110*, B05202, doi:10.1029/2004JB003207.

Hong, T., and C. Marone (2005), Effects of normal stress perturbations on the frictional properties of simulated faults, *Geochem. Geophys. Geosyst.*, 6(3), Q03012, doi:10.1029/2004GC000821.

Humphreys, E. D., and D. D. Coblentz (2007), North American dynamics and western U.S. tectonics, *Rev. Geophys.*, 45, RG3001, doi:10.1029/2005RG000181.

Ide, S., and G. C. Beroza (1997), Does apparent stress vary with earthquake size?, *Geophys. Res. Lett.*, 28(17), 3349–3352.

Jackeiwicz, Z. (1986), Quasilinear multistep methods and variable step predictor-corrector methods for neutral functional differential equations, *SIAM J. Num. Anal.*, 23(2), 423–452.

Johnson, E. (1990), On the initiation of unilateral slip, *Geophys. J. Int.*, 101, 125–132.

Kanamori, H., and D. L. Anderson (1975), Theoretical basis of some empirical relations in seismology, *Bull. Seismol. Soc. Am.*, 65(5), 1073–1095.

Keenan, J. H., F. G. Keyes, P. G. Hill, and J. G. Moore (1978), *Steam Tables*, 156 pp., John Wiley, Hoboken, N. J.

Kostrov, B. V. (1964), Self similar problems of propagation of shear cracks, *J. Appl. Math. Mech.*, 28, 1077–1087.

Lachenbruch, A. H. (1980), Frictional heating, fluid pressure, and the resistance to fault motion, *J. Geophys. Res.*, 85(B11), 6097–6122.

Lachenbruch, A. H., and J. H. Sass (1980), Heat flow and energetics of the San Andreas fault zone, *J. Geophys. Res.*, 85(B11), 6185–6223.

Lachenbruch, A. H., J. H. Sass, G. D. Clow, and R. Weldon (1995), Heat flow at Cajon Pass, California, revisited, *J. Geophys. Res.*, 100(B2), 2005–2012.

Lapusta, N., and J. R. Rice (2003), Low-heat and low-stress fault operation in earthquake models of statically strong but dynamically weak faults, *Eos Trans. AGU*, 84(46), Fall Meet. Suppl., Abstract S51B-02.

Lapusta, N., J. R. Rice, Y. Ben-Zion, and G. Zheng (2000), Elastodynamic analysis for slow tectonic loading with spontaneous rupture episodes on faults with rate- and state-dependent friction, *J. Geophys. Res.*, 105(B10), 23,765–23,789.

Lee, T. C., and P. T. Delaney (1987), Frictional heating and pore pressure rise due to a fault slip, *Geophys. J. Roy. Astr. Soc.*, 88(3), 569–591.

Lim, S. C., and M. F. Ashby (1987), Wear mechanism maps, *Acta Metall.*, 35, 1–24.

Lim, S. C., M. F. Ashby, and J. F. Brunton (1989), The effect of sliding conditions on the dry friction of metals, *Acta Metall.*, 37, 767–772.

Linker, M. F., and J. H. Dieterich (1992), Effects of variable normal stress on rock friction: Observations and constitutive equations, *J. Geophys. Res.*, 97(B4), 4923–4940.

Lykotrafitis, G., A. J. Rosakis, and G. Ravichandran (2006), Self-healing pulse-like shear ruptures in the laboratory, *Science*, 313(5794), 1765–1768, doi:10.1126/science.1128359.

Manighetti, I., M. Campillo, C. Sammis, P. M. Mai, and G. King (2005), Evidence for self-similar, triangular slip distributions on earthquakes: Implications for earthquake and fault mechanics, *J. Geophys. Res.*, 110, B05302, doi:10.1029/2004JB003174.

Mase, C. W., and L. Smith (1985), Pore-fluid pressures and frictional heating on a fault surface, *Pure Appl. Geophys.*, 122, 583–607.

Mase, C. W., and L. Smith (1987), Effects of frictional heating on the thermal, hydrologic, and mechanical response of a fault, *J. Geophys. Res.*, 92(B7), 6249–6272.

Maset, S., L. Torelli, and R. Vermiglio (2005), Runge-Kutta methods for retarded functional differential equations, *Math. Model. Methods Appl. Sci.*, 15(8), 1203–1251.

Matsuzawa, T. (2004), Numerical simulations of the interaction between seismic slip and frictional melting, Ph.D. thesis, Univ. of Tokyo, Tokyo, Japan.

McKenzie, D., and J. N. Brune (1972), Melting on fault planes during large earthquakes, *Geophys. J. R. Astron. Soc.*, 29, 65–78.

Mizoguchi, K., and T. Shimamoto (2004), Dramatic slip weakening of Nojima fault gouge at high-velocities and its implication for dynamic fault motion, *Eos Trans. AGU*, 85(47), Fall Meet. Suppl., Abstract T23A-0559.

Molinari, A., Y. Estrin, and S. Mercier (1999), Dependence of the coefficient of friction on sliding conditions in the high velocity range, *J. Tribol.*, 121, 35–41.

Morgan, J. K., and M. S. Boettcher (1999), Numerical simulations of granular shear zones using the distinct element method: 1. Shear zone kinematics and the micromechanics of localization, *J. Geophys. Res.*, 104(B2), 2703–2719.

Mount, V. S., and J. Suppe (1987), State of stress near the San Andreas fault: Implications for wrench tectonics, *Geology*, 15, 1143–1146.

Nakatani, M. (2001), Conceptual and physical clarification of rate and state friction: Frictional sliding as a thermally activated rheology, *J. Geophys. Res.*, 106(B7), 13,347–13,380.

Nielsen, S., and R. Madariaga (2003), On the self-healing fracture mode, *Bull. Seismol. Soc. Am.*, 93(6), 2375–2388, doi:10.1785/0120020090.

Nielsen, S. B., G. D. Toro, T. Hirose, and T. Shimamoto (2008), Frictional melt and seismic slip, *J. Geophys. Res.*, 113, B01308, doi:10.1029/2007JB005122.

Noda, H. (2004), Numerical simulation of rupture propagation with thermal pressurization based on measured hydraulic properties: Importance of deformation zone width, *Eos Trans. AGU*, 85(47), Fall Meet. Suppl., Abstract T22A-08.

Noda, H. (2008), Frictional constitutive law at intermediate slip rates accounting for flash heating and thermally activated slip process, *J. Geophys. Res.*, 113, B09302, doi:10.1029/2007JB005406.

Noda, H., and T. Shimamoto (2005), Thermal pressurization and slip-weakening distance of a fault: An example of the Hanore fault, southwest Japan, *Bull. Seismol. Soc. Am.*, 95(4), 1224–1233, doi:10.1785/0120040089.

Perrin, G., J. R. Rice, and G. Zheng (1995), Self-healing slip pulse on a frictional interface, *J. Mech. Phys. Solids*, 43, 1461–1495.

Prakash, V. (1998), Frictional response of sliding interfaces subjected to time varying normal pressures, *J. Tribol.*, 120, 97–102.

Prakash, V., and R. J. Clifton (1992), Pressure-shear plate impact measurement of dynamic friction for high speed machining applications, in *Proceedings of the Seventh International Congress on Experimental Mechanics*, pp. 556–564, Society of Experimental Mechanics, Bethel, Conn.

Prakash, V., and F. Yuan (2004), Results of a pilot study to investigate the feasibility of using new experimental techniques to measure sliding resistance at seismic slip rates, SCEC Ann. Prog. Rep., South. Calif. Earthquake Cent., Los Angeles.

Provost, A.-S., and H. Houston (2001), Orientation of the stress field surrounding the creeping section of the San Andreas Fault: Evidence for a narrow mechanically weak fault zone, *J. Geophys. Res.*, 106(B6), 11,373–11,386.

Provost, A.-S., and H. Houston (2003), Stress orientations in northern and central California: Evidence for the evolution of frictional strength along the San Andreas plate boundary system, *J. Geophys. Res.*, 108(B3), 2175, doi:10.1029/2001JB001123.

Rempel, A. W., and J. R. Rice (2006), Thermal pressurization and onset of melting in fault zones, *J. Geophys. Res.*, 111, B09314, doi:10.1029/2006JB004314.

Rice, J. R. (1983), Constitutive relations for fault slip and earthquake instabilities, *Pure Appl. Geophys.*, 121(3), 443–475, doi:10.1007/BF02590151.

Rice, J. R. (1999), Flash heating at asperity contacts and rate-dependent friction, *Eos Trans. AGU*, 80(46), Fall Meet. Suppl., F681l.

Rice, J. R. (2006), Heating and weakening of faults during earthquake slip, *J. Geophys. Res.*, 111(B5), B05311, doi:10.1029/2005JB004006.

Rice, J. R., and S. T. Tse (1986), Dynamic motion of a single degree of freedom system following a rate and state dependent friction law, *J. Geophys. Res.*, 91(B1), 521–530.

Rice, J. R., N. Lapusta, and K. Ranjith (2001), Rate and state dependent friction and the stability of sliding between elastically deformable solids, *J. Mech. Phys. Solids*, 49, 1865–1898.

Richardson, E., and C. Marone (1999), Effects of normal stress vibrations on frictional healing, *J. Geophys. Res.*, 104(B12), 28,859–28,878.

Rockwell, T. K., and Y. Ben-Zion (2007), High localization of primary slip zones in large earthquakes from paleoseismic trenches: Observations and implications for earthquake physics, *J. Geophys. Res.*, 112, B10304, doi:10.1029/2006JB004764.

Ruina, A. (1983), Slip instability and state variable friction laws, *J. Geophys. Res.*, 88(B12), 10,359–10,370.

Saffer, D. M., B. A. Bekins, and S. Hickman (2003), Topographically driven groundwater flow and the San Andreas heat flow paradox revisited, *J. Geophys. Res.*, 108(B5), 2274, doi:10.1029/2002JB001849.

Sagy, A., E. E. Brodsky, and G. J. Axen (2007), Evolution of fault-surface roughness with slip, *Geology*, 35(3), 283–286, doi:10.1130/G23235A.1.

Scholz, C. H. (1982), Scaling laws for large earthquakes: Consequences for physical models, *Bull. Seismol. Soc. Am.*, 72(1), 1–14.

Scholz, C. H. (2000), Evidence for a strong San Andreas fault, *Geology*, 28(2), 163–166, doi:10.1130/0091-7613(2000)28<163:EFASSA>2.0.CO;2.

Scholz, C. H. (2006), The strength of the San Andreas Fault: A critical analysis, in *Earthquakes: Radiated Energy and the Physics of Faulting*, *Geophys. Monogr. Ser.*, vol. 170, edited by R. Abercrombie et al., pp. 301–312, AGU, Washington, D. C.

Scholz, C. H., C. A. Aviles, and S. G. Wesnousky (1986), Scaling differences between large and interplate earthquakes, *Bull. Seismol. Soc. Am.*, 76(1), 65–70.

Segall, P., and D. D. Pollard (1983), Nucleation and growth of strike slip faults in granite, *J. Geophys. Res.*, 88(B1), 555–568.

Sibson, R. H. (1973), Interaction between temperature and pore-fluid pressure during earthquake faulting: A mechanism for partial or total stress relief, *Nature*, *243*, 66–68.

Sibson, R. H. (1975), Generation of pseudotachylyte by ancient seismic faulting, *Geophys. J. R. Astron. Soc.*, *43*, 775–794.

Sibson, R. H. (2003), Thickness of the seismic slip zone, *Bull. Seismol. Soc. Am.*, *93*(3), 1169–1178.

Sirono, S., K. Satomi, and S. Watanabe (2006), Numerical simulations of frictional melting: Small dependence of shear stress drop on viscosity parameters, *J. Geophys. Res.*, *111*, B06309, doi:10.1029/2005JB003858.

Söderlind, G. (2002), Automatic control and adaptive time-stepping, *Numer. Algorithms*, *31*, 281–310.

Spray, J. (1987), Artificial generation of pseudotachylyte using friction welding apparatus: Simulation of melting on a fault plane, *J. Struct. Geol.*, *9*, 49–60.

Spray, J. (1992), A physical basis for the frictional melting of some rock forming minerals, *Tectophysics*, *204*, 205–221.

Spray, J. (1993), Viscosity determinations of some frictionally generated silicate melts: Implications for fault zone rheology at high strain rates, *J. Geophys. Res.*, *98*(B5), 8053–8068.

Spray, J. (1995), Pseudotachylyte controversy: Fact or friction?, *Geology*, *23*, 1119–1122.

Sulem, J., I. Vardoulakis, H. Ouffroukh, and V. Perdikatsis (2005), Thermo-poro-mechanical properties of the aigion fault clayey gouge—application to the analysis of shear heating and fluid pressurization, *Soils Found.*, *45*(2), 97–108.

Suzuki, T., and T. Yamashita (2006), Nonlinear thermoporoelastic effects on dynamic earthquake ruptures, *J. Geophys. Res.*, *111*, B03307, doi:10.1029/2003JB003810.

Tanikawa, W., and T. Shimamoto (2009), Frictional and transport properties of the Chelungpu fault from shallow borehole data and their correlation with seismic behavior during the 1999 Chi-Chi earthquake, *J. Geophys. Res.*, *114*, B01502, doi:10.1029/2008JB005750.

Tavernini, L. (1971), One-step methods for the numerical solution of Volterra functional differential equations, *SIAM J. Numer. Anal.*, *8*(4), 786–795.

Tödheide, K. (1972), Water at high temperatures and pressures, in *Water: A Comprehensive Treatise,* vol. 1, *The Physics and Physical Chemistry of Water*, edited by F. Franks, pp. 463–513, Plenum Press, New York.

Townend, J. (2006), What do faults feel? Observational constraints on the stresses acting on seismogenic faults, in *Earthquakes: Radiated Energy and the Physics of Faulting, Geophys. Monogr. Ser.*, vol. 170, edited by R. Abercrombie et al., pp. 313–327, AGU, Washington, D. C.

Townend, J., and M. D. Zoback (2000), How faulting keeps the crust strong, *Geology*, *28*, 399–402.

Townend, J., and M. D. Zoback (2001), Implications of earthquake focal mechanisms for the frictional strength of the San Andreas Fault system, in *The Nature and Tectonic Significance of Fault Zone Weakening, Geol. Soc. Spec. Publ.*, vol. 186, edited by R. E. Holdsworth et al., pp. 13–21, Geological Society, London, U. K.

Townend, J., and M. D. Zoback (2004), Regional tectonic stress near the San Andreas fault in central and southern California, *Geophys. Res. Lett.*, *31*, L15S11, doi:10.1029/2003GL018918.

Trefethen, L. N. (2000), *Spectral Methods in MATLAB*, SIAM, Philadelphia, Pa.

Tsutsumi, A., and T. Shimamoto (1997), High-velocity frictional properties of gabbro, *Geophys. Res. Lett.*, *24*(6), 699–702.

Tsutsumi, A., S. Nishino, K. Mizoguchi, T. Hirose, S. Uehara, K. Sato, W. Tanikawa, and T. Shimamoto (2004), Principal fault zone width and permeability of the active Neodani fault, Nobi fault system, Southwest Japan, *Tectonophysics*, *379*, 93–108.

Tullis, T. E., and D. L. Goldsby (2003a), Flash melting of crustal rocks at almost seismic slip rates, *Eos Trans. AGU*, *84*(46), Fall Meet. Suppl., Abstract S51B-05.

Tullis, T. E., and D. L. Goldsby (2003b), Laboratory experiments on fault shear resistance relevant to coseismic earthquake slip, SCEC Ann. Prog. Rep., South. Calif. Earthquake Cent., Los Angeles.

Vosteen, H.-D., and R. Schellschmidt (2003), Influence of temperature on thermal conductivity, thermal capacity and thermal diffusivity for different types of rock, *Phys. Chem. Earth*, *28*, 499–509.

Vredevoogd, M., D. Oglesby, and S. Park (2007), Effect of non-linear terms on pore fluid pressurization, in *SCEC Annual Meeting Proceedings and Abstracts*, vol. XVII, p. 188, South. Calif. Earthquake Cent., Los Angeles.

Weldon, R., K. Scharer, T. Fumal, and G. Biasi (2004), Wrightwood and the earthquake cycle: What a long recurrence record tells us about how faults work, *GSA Today*, *14*(9), 4–10, doi:10.1130/1052-5173(2004)014<4: WATECW>2.0.CO;2.

Wibberley, C. A. J. (2002), Hydraulic diffusivity of fault gouge zones and implications for thermal pressurization during seismic slip, *Earth Plant. Space*, *54*(11), 1153–1171.

Wibberley, C. A. J., and T. Shimamoto (2003), Internal structure and permeability of major strike-slip fault zones: the Median Tectonic Line in Mie Prefecture, southwest Japan, *J. Struct. Geol.*, *25*(1), 59–78, doi:10.1016/S0191-8141(02)00014-7.

Williams, C. F., F. V. Grubb, and S. P. Galanis Jr. (2004), Heat flow in the SAFOD pilot hole and implications for the strength of the San Andreas fault, *Geophys. Res. Lett.*, *31*, L15S14, doi:10.1029/2003GL019352.

Yamada, T., J. J. Mori, S. Ide, H. Kawakata, Y. Iio, and H. Ogasawara (2005), Radiation efficiency and apparent stress of small earthquakes in a South African gold mine, *J. Geophys. Res.*, *110*, B01305, doi:10.1029/2004JB003221.

Zheng, G., and J. R. Rice (1998), Conditions under which velocity-weakening friction allows a self-healing versus a cracklike mode of rupture, *Bull. Seismol. Soc. Am.*, *88*, 1466–1483.

Zoback, M. D., and J. H. Healy (1992), In situ stress measurements to 3.5 km depth in the Cajon Pass scientific research borehole: Implications for the mechanics of crustal faulting, *J. Geophys. Res.*, *92*(B1), 5039–5057.

Zoback, M. D., et al. (1987), New evidence for the state of stress on the San Andreas fault system, *Science*, *238*, 1105–1111.

E. M. Dunham, Department of Earth and Planetary Sciences and School of Engineering and Applied Sciences, Harvard University, 288 Pierce Hall, 29 Oxford Street, Cambridge, MA 02138, USA. (edunham@fas.harvard.edu)

H. Noda, Seismological Laboratory, California Institute of Technology, 1200 E California Boulevard, Mail Code 252-21, Pasadena, CA 91125, USA. (hnoda@caltech.edu)

J. R. Rice, Department of Earth and Planetary Sciences and School of Engineering and Applied Sciences, Harvard University, 224 Pierce Hall, 29 Oxford Street, Cambridge, MA 02138, USA. (rice@esag.harvard.edu)